Scaling investigation of plasma-induced flows over curved and flat surfaces: Comparison to the wall jet

S. Baleriola, A. Leroy, S. Loyer, Philippe Devinant, Sandrine Aubrun-Sanches

Version of Record: https://www.sciencedirect.com/science/article/pii/S0142727X18304284
Manuscript_ff7821d3ef84d78afdc46f7471910857

Scaling investigation of plasma-induced flows over curved and flat surfaces: comparison to the wall jet

S. Baleriola[a], A. Leroy[a,*], S. Loyer[a], Ph. Devinant[a], S. Aubrun[b]

[a] *Université d'Orléans, INSA-CVL, PRISME, EA 4229, 45072 Orléans, France*
[b] *Ecole Centrale de Nantes, LHEEA, UMR CNRS 6598, 44321 Nantes, France*

Abstract

The present investigation deals with Dielectric Barrier Discharge (DBD) induced jets flowing over curved surfaces and studied in the framework of a circulation control application, carried out by acting near the rounded trailing-edge of an airfoil. These jets are characterised experimentally via Particle Image Velocimetry (PIV) in quiescent air conditions. The study assesses the evolution of these flows in terms of self-similarity of the mean flow and of its turbulent components. DBD wall jets evolution in the streaming direction is also analysed through the rate of spread and the maximum velocity decay evolution as commonly done for fluidic wall jets, and also through several normalised quantities deriving from different length and velocity scales. A comparison with a canonical flow, such as the classical wall jet flowing over plane or curved surfaces, is made in order to find out the similarities and the discrepancies between these two flows. Results reveal that DBD wall jets and canonical fluidic wall jets show comparable properties in the diffusion zone. Compared to the plane DBD wall jet, centrifugal forces are responsible of the greater spread of curved DBD wall jets and are likely the source of instabilities leading to their transitional state. The momentum flux of the induced jet and the radius of curvature of the surface are two relevant scales for DBD induced flows developing over curved surfaces.

Keywords: DBD, curvature effect, plasma wall jet

1. Introduction

In the field of active flow control, plasma-based actuators are widely used to achieve flow manipulation and enhance aerodynamic performances over a large range of applications (e.g., aerospace, wind energy, aeronautics, turbomachinery). However, these kinds of actuators are not yet mature for industrial applications as reported in Kriegseis et al. (2016). Nevertheless, surface plasma actuators based on a Dielectric Barrier Discharge (DBD) are frequently studied because of their easy implementation, short time-response and versatility. In the domain of flow control over airfoils, many studies have analysed the aerodynamic effects of this actuation which can be used to successfully achieve boundary layer separation control (Post and Corke (2004)), circulation control by acting near a rounded trailing-edge (Zhang et al. (2011), Meijerink and Hoeijmakers (2011), Kotsonis et al. (2014) and Baleriola et al. (2016)) or by the implementation of Gurney flaps with plasma induced jets (Feng et al. (2015)), and boundary layer transition control (Schuele et al. (2013), Lovig et al. (2014) and Yadala et al. (2018)) among others.

As in all flow control studies, the analysis in quiescent air conditions of the flow induced by DBD actuators needs to be carried out to characterise the induced jet development over the model surface and to investigate the mechanisms of interaction with the external flow. Furthermore, this kind of characterisation is helpful for the implementation and validation of phenomenological models (Shyy et al. (2002), Suzen et al. (2005)), PIV-based computational methods (Maden et al. (2013)) or physics-based approaches (Boeuf et al. (2007), Rogier et al. (2014)) that seek to numerically reproduce the DBD induced flows involved in flow control applications. Indeed, it is relevant to determine if classical laws used to model DBD induced jets and based on plane wall jet analogies are still valid for less conventional surfaces such as curved ones. This characterisation also provides the induced jet velocity profile evolution as a function of the applied voltage, which is necessary to estimate the momentum coefficient, commonly used to assess the strength and efficiency of the actuation as done in Sosa et al. (2007) and Kotsonis et al. (2014), for example.

Previous studies in quiescent air are conducted with actuators implemented on a flat configuration. However, as far as DBD circulation control over an airfoil with a rounded trailing-edge is concerned, it is necessary to study the development of the induced flow evolving along a curved wall. It is within this framework that the present study was carried out. To investigate experimentally, at a wind-tunnel scale, the airfoil lift increase or decrease, DBD plasma actuators were implemented over an airfoil

*Corresponding author
Email address: annie.leroy@univ-orleans.fr (A. Leroy)

model designed with a specific rounded trailing-edge (TE) as reported in Baleriola et al. (2016). Due to the dimensions of the model designed for wind-tunnel tests, the curvature radius of the rounded trailing-edge is of an order of magnitude equal to a few millimeters. More conventional circulation control strategies are traditionally implemented by means of concepts including shape change, TE flaps or air blowing and often rely on the Coanda effect that keeps a tangential jet attached over a curved surface. Whereas blowing techniques usually show high momentum coefficients (Joslin and Jones (2006)), it is not possible to achieve similar performances so far with DBD actuators due to their inherent limitation to produce a high level of momentum, in spite of the promising outcomes of the numerical approach proposed by Zhang et al. (2010). According to Joslin and Jones (2006) and demonstrated by Kotsonis et al. (2014) and Baleriola et al. (2016), lift increase achieved thanks to circulation control is mainly due to a mechanism of boundary layer separation manipulation around the trailing-edge which modifies the mixing of the near wake without totally suppressing it. Nevertheless, by considering specific arrangements of electrodes, it is possible to produce a tangential jet over a curved wall with a small radius of curvature that will stay more or less attached to the surface. Several DBD actuators were used for the intended flow control application. Their induced flows were characterised in quiescent air conditions and constitute the working basis of this study.

Generally, DBD induced jets are compared to fluidic wall jets even if some differences remain between them. In the case of a DBD induced jet, the electrically charged particles close to the wall are accelerated from the active electrode and along the grounded one, following the electrical field. This particle motion entrains the ambient air in the same direction along the wall, creating an induced jet. There is no nozzle or jet exit and the flow accelerates continuously until roughly the end of the last grounded electrode. The velocity magnitude induced by a single DBD is weak (max. $\approx 8\,\mathrm{m/s}$ as in Moreau (2007)) compared to most fluidic jets. In the case of a DBD induced jet, there is no mass addition by the actuator but only mass entrainment and momentum transfer.

The present study focuses on the experimental characterisation by PIV (Particle Image Velocimetry) of the plasma induced jets evolving along a specific airfoil with a rounded trailing-edge as a function of the electrode arrangement and without an external flow. In order to highlight the effects of possible centrifugal forces on curved induced jets, a DBD induced jet in a flat configuration equivalent to the curved ones was also studied. Induced jets main features were analysed by using dimensional and normalised variables commonly used for fluidic wall jets. This approach made it possible to assess the transition of such plasma induced jets from a laminar to a turbulent regime and to evaluate the evolution of DBD induced flows in terms of self-similarity of the mean flow and of its turbulent components as well as in terms of rate of spread and maximum velocity decay evolution. Furthermore, this analysis enabled us to determine whether or not plasma induced jets show similar properties as canonical fluidic wall jets but also to determine which are the most relevant variables to describe the evolution of the jets along a curved wall. The causes leading to the jet transition to turbulence were also investigated.

First, a short review of previous investigations on fluidic wall jets and on DBD induced jets is presented to introduce the comparison between these two flows. Then, the mean topology of curved DBD flows is analysed for three actuator positions around the airfoil trailing-edge. The third part establishes the basis for the fourth section that studies the streamwise evolution of the induced jets in the jet-related coordinate system.

1.1. Fluidic wall jets

Förthmann (1936) studied the wall jet (WJ) for the first time and theoretically compared it to the free open jet. Assuming x as the WJ streaming direction, the author proved that the jet maximum velocity decreases as $x^{-\frac{1}{2}}$ and that the jet spread, defined as the maximum velocity half-width, linearly evolves along the x-direction. In addition, velocity profiles from different distances to the nozzle proved to be coincident in one curve showing a similarity law.

A wall jet can be divided into two distinct layers on both sides of the velocity peak as introduced by Glauert (1956). On the one hand, the inner layer is located between the wall and the maximum velocity ordinate. Due to the influence of the wall, Glauert (1956) predicted that this zone would behave as a turbulent boundary layer, whereas the outer layer would be similar to the shear layer of a free jet. As the WJ develops, the inner layer becomes wider and the maximum velocity decreases. However, jet velocity decreases faster than spread increases. This implies that the local Reynolds number of the jet, based on the maximum jet velocity and its related velocity half-width, slowly decreases with the jet development.

The wall jet development can also be described in the streamwise direction and be characterised by three distinct zones: the potential core, where the nozzle exhaust velocity is preserved; a transitional region where the flow shifts progressively from a laminar to a turbulent regime, and a fully developed zone where the flow is completely turbulent. One of the main difficulties is to determine the critical jet Reynolds number Re_{jc} corresponding to the transitional regime. Kurtz and Crandall (1962) studied theoretically the natural convection on a heated vertical plate on air and found a Re_{jc} of 161. Chun and Schwarz (1967) carried out a theoretical study on the stability of an incompressible, viscous plane WJ subjected to small disturbances and Re_{jc} was determined to be about 57. An experimental stability investigation of a laminar two-dimensional plane WJ was carried out by Bajura and Szewczyk (1970). The authors concluded that

the critical value of Re_{jc} lies between 500 and 2000. Bajura and Catalano (1971) studied a transitional plane WJ (Reynolds number between 100 and 600) and found that Kelvin-Helmholtz instability of the free shear layer plays an important role in the WJ transition. Schneider and Goldstein (1994) carried out a detailed analysis on the turbulent WJ evolution with three different measurement techniques (pressure probe, Laser Doppler Anemometry and Hot Wire Anemometry).

Bradshaw and Gee (1960) carried out experiments on a WJ developing over a circular cylinder. The growth of the curved WJ thickness proved to be linear and equal to 1.5 times that of the plane WJ. According to the authors, this thickness increase may be caused by a negative radial gradient of angular momentum that causes a centrifugal instability on the turbulent flow. The authors defined an angle θ^* from the nozzle to the azimuthal position of the velocity profile. In their experiment, the curved WJ remained attached to the wall until an angle θ^* of 150°. An in-depth study on the plane WJ was carried out by Wygnanski et al. (1992) and pursued by Neuendorf and Wygnanski (1999) who also examined the WJ development around a circular cylinder. The rate of spread and the velocity decay of the curved WJ appeared to be greater than those of the plane WJ, as were the levels of turbulence and Reynolds stresses.

1.2. Wall jets induced by DBD actuators

Wall jets induced by DBD actuators (DBD-WJs) have been studied only on plane configurations. Table 1 shows a summary of DBD-WJ characteristics found in the literature. Only publications showing velocity profile investigations relevant to this study are cited. The table specifies the type of actuator, the method used for the measurement of the velocity profiles, the maximum jet velocity U_j and its corresponding thickness (maximum velocity half-width) b and jet Reynolds number Re_j. A precise definition of these variables is given below in section 3.1. For thick dielectrics (thicker than 2 mm) the jet velocities are between 3 and 5 m/s and jet thicknesses between 2 mm and 5 mm at the end of the last grounded electrode (beginning of jet diffusion). This leads to Reynolds numbers from 400 to 900 suggesting that the plane DBD induced jets found in the literature are laminar or in a transitional regime. DBD-WJs seem to be similar to laminar WJs as pointed out by Roth et al. (2004) and Jukes et al. (2006). As for fluidic WJs, jet velocity decay seems to evolve as $x^{-\frac{1}{2}}$ and jet thickness as $x^{\frac{3}{4}}$ (or x). Murphy et al. (2013) found that as the voltage is increased, and hence the Reynolds number, the velocity peak of the velocity profile shifts closer to the wall. The authors also calculated the evolution of the standard deviation of the longitudinal velocity σ_u for a large range of Reynolds numbers and found a σ_u increase with Re_j up to a Reynolds number of 100. Beyond this value a σ_u plateau was reached. The authors suggested that the WJ generated by a DBD actuator becomes turbulent at $Re_{jc} \approx 100$. In Maden et al. (2013) the authors used PIV measurements and numerical computations to study DBD-WJs. Their Re_j was about 370 and the velocity peak location moved towards the wall as the jet developed. Boucinha et al. (2008a), Murphy et al. (2013) and Maden et al. (2013) found the maximum velocity ordinates between laminar and turbulent WJ profiles. DBD induced flows have low Reynolds numbers and appear to be laminar although some instabilities exist and natural transition may occur downstream of the actuator, as with other dynamic flow control devices.

2. Mean topology of the flow induced by a DBD actuator along a curved surface

2.1. Experimental set-up

The airfoil used for the flow control application was a NACA65$_4$-421 airfoil with a rounded trailing-edge as employed in Baleriola et al. (2016) for circulation control. The model has a chord c equal to 0.3 m and is 1.1 m wide. The radius of curvature R of the TE is 2% of the chord (6 mm). The model (figure 1) is composed of a front main part, from the leading-edge to 70% of the chord, and of a removable trailing-edge. The trailing-edge is itself composed of a holder and a cap both made of PMMA.

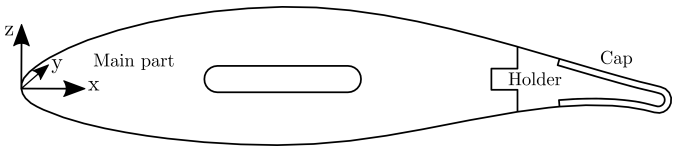

Figure 1: Side view of the model

2.1.1. DBD plasma actuators

Figure 2 shows the top view and the geometry of the electrodes of the actuators used. The grounded electrodes are linear (strip electrodes) and 12 mm wide. The high voltage electrodes are serrated (triangular pattern in series) in order to ensure plasma homogeneity along the wingspan and to avoid uneven discharge distributions (Matsuno et al. (2016)) in the intended flow control application. All the actuators used are made up of two single DBD actuators in a row. All the electrodes used are copper electrodes (85 µm thick) and are separated by the 3 mm-thick PMMA dielectric of the model cap. The use of a thick dielectric allows the generation of a thicker induced wall jet with higher jet velocities compared to thin dielectrics. The grounded electrodes are encapsulated by the dielectric of the model itself (holder part). To prevent plasma formation in the opposite flow direction, active electrodes are partly covered with a layer of polyimide film. The spanwise length of the actuators is 900 mm.

Three positions of the multi-DBD actuator were studied and are shown in figure 3. The electrode arrangement and the distances between the electrodes are identical for the three positions, the only difference is their position

Publication	Actuator type	Method	U_j[m/s]	$b[mm]$	Re_j
Roth et al. (2004)	SDBD (ceramic, 0.635 mm)	PP	3.2	2	410
Pons et al. (2005)	SDBD (glass, 4 mm)	PP	3.25	2.5	520
Jukes et al. (2006)	Symmetric DBD (Mylar, 250 µm)	HWA	0.51	1.3	45
Forte et al. (2007)	SDBD (glass, 2 mm)	PP	4	2	510
Boucinha et al. (2008a)	SDBD (Mylar and Kapton, 0.7 mm)	LDV	3.8	1	240
Moreau et al. (2008)	Sliding DBD (PMMA, 4 mm)	PP	4.2	3	800
Balcon et al. (2009)	SDBD (PMMA, 3 mm)	PIV	2.7	5	860
Benard et al. (2009)	S2DBD (PMMA, 3 mm)	PP	3.8	1.7	410
Debien et al. (2011)	ExDBD (PMMA, 3 mm)	PIV	4.2	3	800
Durscher and Roy (2012)	SDBD (acrylic, 3 mm)	PIV & PP	4	2	510
Erfani et al. (2012)	SDBD (Kapton, 0.3 mm)	PIV	1.2	2	150
Maden et al. (2013)	SDBD	PIV & num.	-	-	370
Murphy et al. (2013)	SDBD (Kapton, 0.36 to 0.45 mm)	PIV	-	-	20-250
Benard and Moreau (2014)	SDBD (PMMA, 3 mm)	PP	5	2.8	900
Belan and Messanelli (2015)	Serrated SDBD (PMMA, 2 mm)	PP	3.2	1.5	300

Table 1: Overview table of plane DBD-WJ characteristics from previous studies (SDBD: Single DBD, S2DBD: Single two-electrode DBD, ExDBD: Extended DBD)

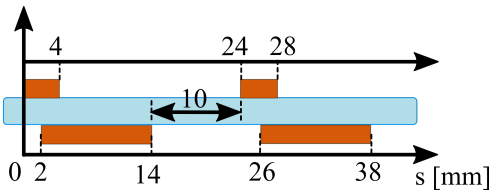

(a) Geometry of a plane multi-DBD actuator

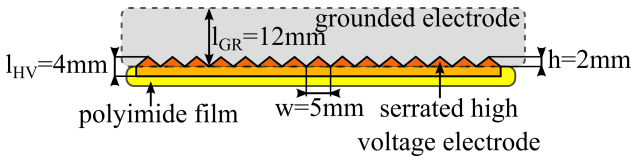

(b) Top view of the electrodes

Figure 2: Geometry and top-view of the electrodes

around the trailing-edge of the airfoil. The actuator implemented in *position A* starts blowing well before the TE curvature and its second active electrode is located before the curvature. The electrodes corresponding to *position B* are centered on the middle line of the TE, the second active electrode being just before its center line. *Position C* has its set of electrodes shifted by an angle of 45° towards the lower side of the airfoil with respect to the TE center line. An equivalent plane configuration was also tested for comparison with the curved induced jets.

These actuators are intended to perform circulation control: two actuators were designed to increase the lift force (*Pos. B* and *Pos. C*) and one to decrease it (analogous to *Pos. C* but blowing in the opposite direction, from the lower side to the upper side of the airfoil). The effectiveness of the actuation was proved through load and pressure measurements and a lift coefficient increase of about ± 0.1 was performed in the linear part of the lift curve. The whole pressure distribution around the airfoil was modified despite the fact that the action takes place solely at the trailing-edge. The input electrical parameters (voltage and frequency) employed in this study correspond to this flow control application.

2.1.2. *Electrical set-up*

The power supply employed is a laboratory-made supply composed of a Crown amplifier (XS1200 series, 22 Hz - 22 kHz, 2.3 kW) and of a single-phase transformer made by Trabo (90 V - 20 kV, 2 kW, 20 Hz - 20 kHz). The maximum voltage output is about 20 kV and 2 kW. The sinusoidal function generator is a TTi (TGA1241, 40 MHz, 10 V). The applied high voltage is measured with a high voltage Tektronix probe (P6015A series, 75 MHz, 3 pF).

2.1.3. *PIV set-up*

The actuators were characterised in quiescent air conditions using a PIV system. Trailing-edges were tested inside an enclosed box (1.1 m × 0.5 m × 0.5 m) with a seeding arrival and an aspiration system that can remove seeding particles if required. The laser is a Nd:Yag Quantel Twins (Ultra series, 2 × 200 mJ, 532 nm) coupled with a laser sheet generator lens. Images were recorded with a TSI PowerView 4M Plus camera with a sensor size of 2048 px × 2048 px and equipped with a Nikon 200 mm focal length objective set at an f-number of 5.6. Image pairs were recorded at a frequency of 4 Hz and were analysed with the Insight 4G software of TSI. In the case of the curved configurations, the final interrogation window was 32 px × 32 px and an overlap factor of 50% was used. The dimensions of the field of view were 60 mm × 60 mm and the vector fields were produced at a final resolution

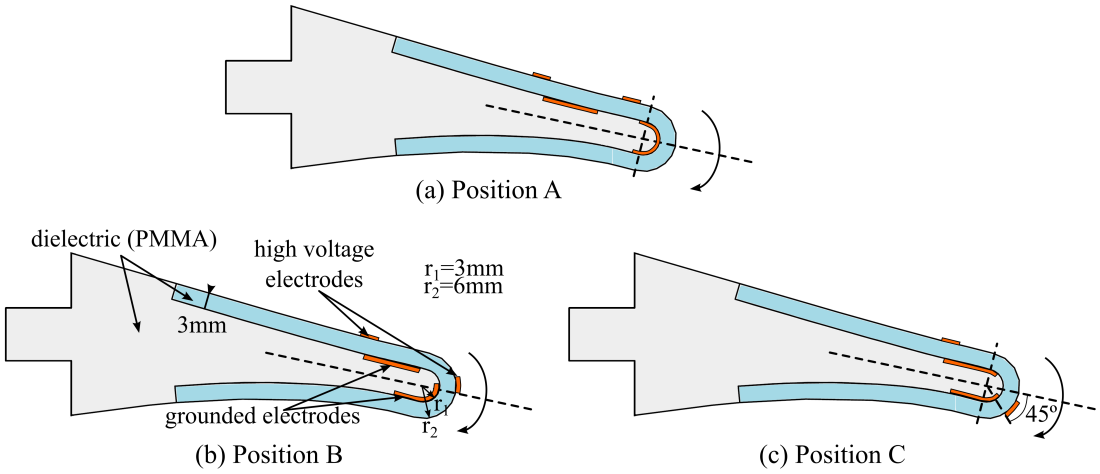

Figure 3: Drawing of electrode position around the trailing-edge of the airfoil

of 0.47 mm/vec (0.03 mm/px). Time averaging was performed with 600 image pairs. PIV analysis of the plane configuration was performed with different set-up parameters due to the ensuing different geometry. The dimensions of the field of view were 102 mm × 102 mm and the final interrogation window was 16 px × 16 px with an overlap factor of 50%. The final resolution was 0.4 mm/vec (0.05 mm/px). Time averaging was performed with 1000 image pairs. In both cases, seeding particles were micro-sized olive oil droplets sprayed by a PIVTEC seeding system with a particle diameter of 1 µm. The flow induced by the plasma actuator is assumed to be two-dimensional and PIV measurements were carried out in the plane of symmetry of the airfoil TE or of the plane induced jet. In both plane and curved configurations statistical convergence for the mean flow and of its turbulent components was reached.

As mentioned in Prasad (2000), PIV errors can be decomposed in: (1) random errors, (2) bias errors, (3) gradient errors, (4) tracking errors and (5) acceleration errors. With the exception of random and bias errors, these errors are not deterministic and it is therefore difficult to give a quantitative estimation of the overall systematic errors on the measured velocity fields. However, experiments were carried out carefully in order to minimise these errors. Wall reflections were reduced with the use of non-reflective coatings and the ensemble average of minimum intensity was subtracted from the raw images during the pre-processing as mentioned in Kotsonis (2015). Also, particle diameter was equal to about 2 px as suggested in Prasad (2000). The frame time interval was chosen such as particles are displaced of $\frac{1}{4}$ of the final interrogation window as mentioned in Keane and Adrian (1990). Furthermore, during the post-processing, two passes were used with decreasing interrogation areas and a 50% overlap as also advised in Prasad (2000). Vectors were accepted if the ratio between the 1st and the 2nd correlation peaks was above 1.2 and a median filter was applied to the resulting velocity field.

To quantify random errors, statistical uncertainty of the mean velocity can be computed using the central limit theorem (Coleman and Steele (2009)). This method was recently used by Van Hooff et al. (2012) and Kaffel et al. (2015) for the evaluation of the repeatability error of PIV measurements on a plane WJ in a confined space and a plane WJ subjected to an external lateral flow respectively. The statistical error $\widetilde{u_r}$ is defined as:

$$\widetilde{u_r} = \frac{1}{\sqrt{N_s}} z_{\frac{\alpha}{2}} \frac{U_{RMS}}{U} \tag{1}$$

where N_s is the number of samples, $z_{\frac{\alpha}{2}}$ is equal to 1.96 for a confidence interval of 95%, U_{RMS} is the local root mean square velocity and U the mean velocity at the same location. The uncertainty calculated in the worst configuration (maximum U_{RMS}) was about 2% for the plane configuration and 3.5% for the curved ones.

2.2. Mean topology in the airfoil-related coordinate system

The airfoil-related coordinate system, named (x, y, z), is defined as: x-axis in the direction of the airfoil chord, y-axis in the wingspan direction and z-axis in the vertical direction (see figure 4a). Velocity average and fluctuating parts are defined according to the following Reynolds decomposition where t represents the time dependency: longitudinal velocity defined as $U(x,z,t) = \overline{U}(x,z) + u'(x,z,t)$ and vertical velocity as $V(x,z,t) = \overline{V}(x,z) + v'(x,z,t)$.

Figure 4 shows time-averaged velocity magnitude fields for the three configurations tested. Electrode position and geometry are superimposed in the figures. Normal velocity profiles are also plotted and are computed with a linear interpolation in the normal direction to the wall using a spatial step equal to the PIV resolution (0.47 mm/vec). Even though the three actuators are powered at the same

voltage V_{AC} and frequency f_{AC} (and therefore consume the same electrical power), the three curved DBD-WJs topologies are significantly different.

The induced WJ corresponding to *Pos. A* starts well before the trailing-edge curvature, develops along the upper side of the airfoil and starts deflecting over the second grounded electrode. This curved DBD-WJ does not follow the TE curvature and detaches perpendicularly to the airfoil chord, along the z-direction. The induced flow of *Pos. B* partially follows the TE curvature but does not remain perfectly attached to the model. On the contrary, the DBD-WJ in *Pos. C* follows the wall curvature and perfectly adheres to the model wall beyond the 180° sharp turn. This different jet behaviour can be explained by the electrode arrangement of the three actuators. For *Pos. A*, the actuator ends too early to allow the TE circumvention. In the cases of *Pos. B* and *Pos. C*, the region of EHD interaction reaches the end of the TE curvature and the WJ is forced to completely follow the sharp turn curvature. However, the zone of EHD interaction of *Pos. C* reaches the lower side of the airfoil and the induced jet can remain perfectly attached to the model wall.

Electrode position has a direct impact on the DBD-WJ topology, in particular on whether the induced jet is going to follow the model curvature or not. The reason why DBD-WJs stay attached to the wall seems to be more an electrical effect than a phenomenon due to the dynamics of the fluid. Fekete (1963) studied the Coanda effect of a WJ over a cylinder and pointed out that a complete circumvention (separation at an azimuthal angle from the nozzle of 180°) occurs with high Reynolds numbers (over 20 000) and small ratios $\frac{b}{R}$, b being the jet half-width and R the radius of curvature of the cylinder. The angle of separation θ_{sep} rapidly increases with the Reynolds number and tends to stabilize at $Re_j = 30\,000$ at about 210°. For low Reynolds numbers and ratios $\frac{b}{R}$ under 0.05, the author found θ_{sep} equal to 60°, 75°, 100° and 140° for Re_j equal to 1500, 2000, 2500 and 5000 respectively. In the present configuration, a curved DBD-WJ has a ratio $\frac{b}{R}$ before reaching the TE equal to 0.66 which is quite a high value. Vít and Maršík (2004) studied a heated Coanda laminar WJ and for Re_j of 740 and 950 obtained an angle θ_{sep} of 40° and 90° respectively for a ratio $\frac{b}{R} = 0.25$. Their results showed that over this ratio separation occurs at even smaller θ angles. Hence, the Coanda effect does not seem to be applicable for the curved DBD-WJs of the present study in view of the Reynolds numbers and jet thicknesses involved.

3. Two-dimensional wall jet developing along plane or curved surfaces

This section establishes the nomenclature used in the following analysis and introduces the necessary variables.

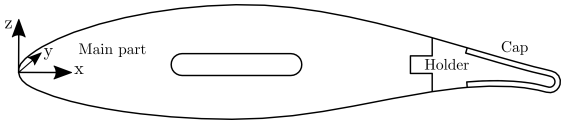

(a) Airfoil-related coordinate system

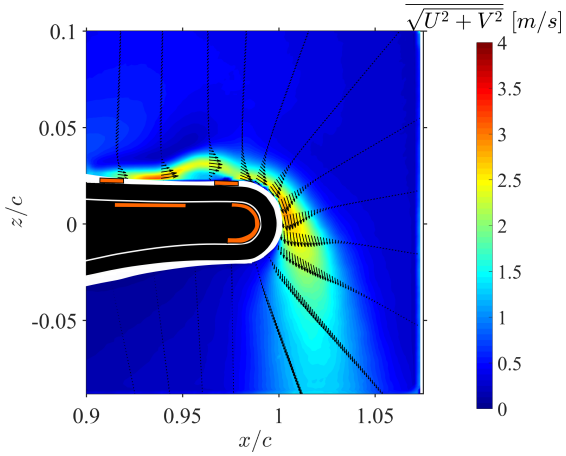

(b) Pos. A

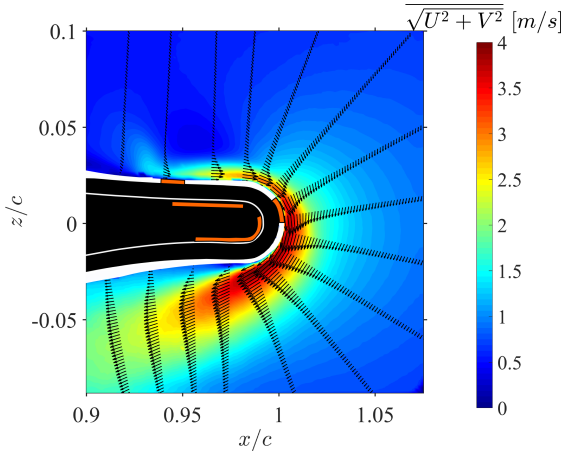

(c) Pos. B

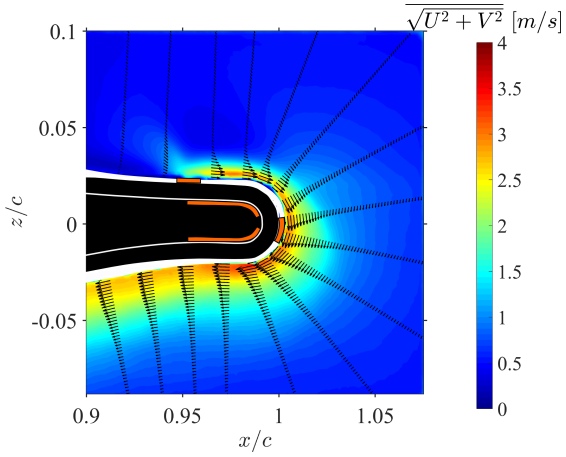

(d) Pos. C

Figure 4: Time-averaged velocity fields for the three electrode positions in quiescent air conditions ($V_{AC} = 18\,\text{kV}$ and $f_{AC} = 1\,\text{kHz}$)

3.1. Plane and curved wall jet variables

To analyse the wall jet development over a plane surface some quantities are usually defined as shown in figure 5. A new coordinate system related to the WJ and different from the one presented in the section above is defined here. It is defined in such a way that the abscissa x is in the longitudinal direction of the flow and the ordinate z in the normal direction. The origin of the x-coordinate is the exit of the nozzle and the z-coordinate origin is the surface of the wall. Each velocity profile along the x-coordinate has its local maximum velocity named $U_{max}(x)$ located at a distance $z_{max}(x)$ from the wall. The variable $z_{\frac{1}{2}}(x)$ is defined as the distance from the wall to the location at which the mean velocity decreases to one half of its local maximum value in the outer flow. The jet maximum velocity U_j is the jet velocity slightly downstream of the exit of the nozzle, at the x_0 abscissa defined as $U_{max}(x_0) = U_j$. The Reynolds number of the jet is defined as $Re_j = \frac{U_j b}{\nu}$ where b is the nozzle width and ν is the kinematic viscosity of the flow. In the case of a plane DBD-WJ (see figure 6), as there is no physical nozzle, the origin of the x coordinate ($x = 0$) is set at the beginning of the first active electrode and the abscissa of the virtual origin x_0, corresponding to the maximum jet velocity, is also defined as $U_{max}(x_0) = U_j$. The virtual slot width b is defined as the jet thickness at the virtual origin $b = z_{\frac{1}{2}}(x_0)$. Assuming that the surface discharge has a negligible effect on the gas properties as mentioned in Moreau (2007), the kinematic viscosity of the induced jet is assumed to be equal to the kinematic viscosity of air. Then, the jet Reynolds number Re_j can be defined by analogy with the fluidic WJ defined above.

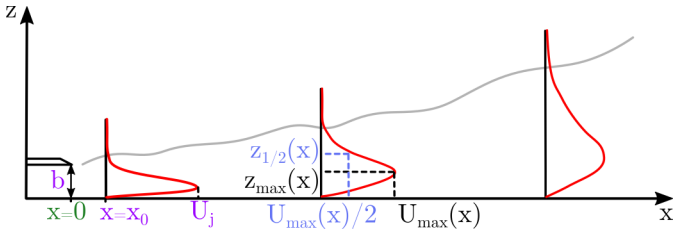

Figure 5: Scheme of a fluidic plane WJ over a plane surface and its specific variables

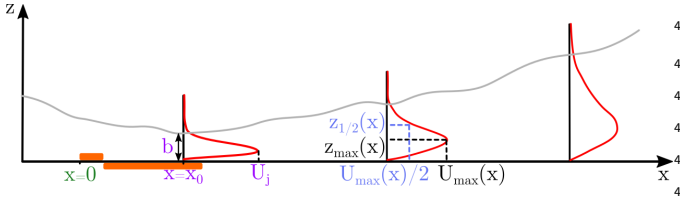

Figure 6: Scheme of a DBD-WJ over a plane surface and its specific variables

A second coordinate system is defined to follow a wall jet evolution over a curved surface. Neuendorf and Wygnanski (1999) studied a WJ flowing around a circular cylinder and defined an angle θ^* (figure 7a) between the nozzle and the azimuthal position of the velocity profile. In the present case (figure 7b), as the trailing-edge is not axisymmetric, a curvilinear abscissa x^* is defined along the curvature with a related vertical coordinate z^* normal to the model wall. The origin of the x^* coordinate ($x^* = 0$) is set at the beginning of the actuator (first active electrode). Variables $z^*_{max}(x^*)$, $U_{max}(x^*)$ and $z_{\frac{1}{2}}(x^*)$ are defined in the same way as for the plane WJ described above. Local variables such as the maximum jet velocity U_j, the virtual origin x^*_0, the virtual slot width b^* and the jet Reynolds number Re_j are also defined in accordance with the plane case. The angle β is defined as the angle between the trailing-edge extremity and the virtual origin x^*_0.

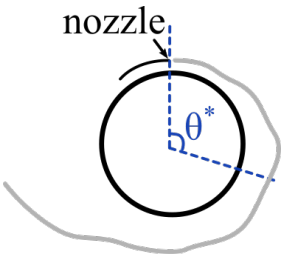

(a) Angle θ^* definition

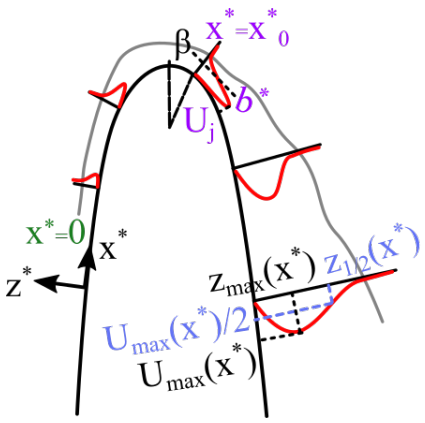

(b) Scheme of a DBD-WJ over a curved surface

Figure 7: (a) θ^* angle definition over a cylinder, (b) Scheme of a DBD-WJ over a rounded trailing-edge and its specific variables

3.2. Scalings

Three different scalings will be considered in the following and are summarized in table 2. The first scaling (scaling 1) is the conventional normalisation that considers the virtual slot width b (or b^*) as the length scale and the jet velocity U_j as the velocity scale. In Wygnanski et al. (1992) the authors demonstrated that self-similarity of a plane WJ depends on the momentum flux J as well as on the viscosity and density of the fluid leading to the second scaling (scaling 2): $\frac{\nu^2}{J}$ is the length scale and $\frac{J}{\nu}$ the velocity scale. The authors in Neuendorf and Wygnanski (1999) suggested a new normalisation for curved

	Scaling 1 (plane & curved WJ)	Scaling 2 (plane & curved WJ)	Scaling 3 (curved WJ)
Length scale	b	$\frac{\nu^2}{J}$	R
Velocity scale	U_j	$\frac{J}{\nu}$	$\sqrt{\frac{J}{R}}$
Jet Re	$Re_j = \frac{bU_j}{\nu}$	—	$Re_N = \frac{\sqrt{JR}}{\nu} = \sqrt{\frac{\frac{1}{2}U_j^2 b^* R}{\nu^2}}$
Local Re	$Re_x = \frac{U_{max}(x) z_{\frac{1}{2}}(x)}{\nu}$	—	$Re_N(x^*) = \frac{\sqrt{J(x^*)R}}{\nu}$

Table 2: Summary of the three employed scalings

WJs (scaling 3) involving the radius of curvature R as the length scale and $\sqrt{\frac{J}{R}}$ as the velocity scale. For both scalings 2 and 3 the kinematic momentum flux $J(x)$ (or $J(x^*)$) is defined as:

$$\begin{aligned} J(x) &= \int_{z=0}^{\infty} U^2(x,z)dz \\ &= z_{\frac{1}{2}}(x)U_{max}^2(x) \underbrace{\int_{\frac{z}{z_{\frac{1}{2}}}=0}^{\infty} \left(\frac{U(x,z)}{U_{max}(x)}\right)^2 d\left(\frac{z}{z_{\frac{1}{2}}}\right)}_{K(x)\approx constant} \quad (2) \\ &= z_{\frac{1}{2}}(x)U_{max}^2(x)K(x) \end{aligned}$$

which gives at the nozzle or virtual origin x_0 (or x_0^*):

$$J_0 = J(x_0) \quad (3)$$

$$= z_{\frac{1}{2}}(x_0)U_{max}^2(x_0) \underbrace{\int_{\frac{z}{z_{\frac{1}{2}}}=0}^{\infty} \left(\frac{U(x_0,z)}{U_{max}(x_0)}\right)^2 d\left(\frac{z}{z_{\frac{1}{2}}}\right)}_{K(x_0)=K_0} \quad (4)$$

$$= bU_j^2 K_0 \quad (5)$$

It should be noted that J_0 is a constant for a given induced jet whereas $J(x)$ is a local variable that evolves with the WJ development. For scaling 3, the authors redefined the Reynolds number as $Re_N = \frac{\sqrt{JR}}{\nu}$.

4. Characterisation of DBD wall jets in the jet-related coordinate system

4.1. Jet main characteristics

Table 3 shows the DBD induced jet characteristics for the actuators studied. The Reynolds numbers of the jets are shown according to the two definitions specified in table 2.

In the case of *Pos. A* powered at 18 kV, the virtual origin x_0^* is located at an angle β with respect to the TE extremity equal to $-10°$ whereas for *Pos. B* and *Pos. C* it is located at 60° and 70° respectively. The position of the virtual origin is directly related to the WJ topology and therefore to the position of the electrodes around the TE: the more the DBD-WJ attaches to the model curvature, the greater the β angle. While the jet velocity magnitude U_j is equivalent between plane and curved DBD-WJs, the jet thickness b (or b^*) remains smaller for the plane cases leading to lower Reynolds numbers. The Reynolds number Re_j for curved DBD-WJs varies from 1100 to 1900 whereas the one according to Neuendorf's definition Re_N ranges from 900 to 1200 and is more uniform for all the actuators and voltages tested. This is due to the magnitude of the length scales b and $\sqrt{bR}$ used in the Reynolds numbers Re_j and Re_N. In our case $b \approx 7$ mm and $\sqrt{bR} \approx 6.6$ mm which leads to a Re_N slightly smaller than Re_j. This is not the case in Neuendorf and Wygnanski (1999) where Re_N is almost five times higher than Re_j because $b \approx 2.3$ mm and $\sqrt{bR} \approx 15$ mm. Whatever the Reynolds number definition used, all the DBD induced jets are in a transitional regime or not very far from it according to the critical Reynolds number suggested by Murphy et al. (2013) which is $Re_{jc} \approx 100$ for DBD induced jets.

4.2. Self-similarity of the mean velocity profiles and of the turbulent components

The objective of this section is to characterise the curved and plane induced jets in terms of velocity profiles and self-similarity. Both plane and curved DBD-WJs are powered at $V_{AC} = 18$ kV but have distinct Reynolds numbers: 600 for the plane DBD and 1300 for the curved DBD in *Pos. C*. The latter curved case behaves the closest to the plane WJ of all the curved actuators studied, especially in the diffusion zone. Velocity profiles normal to the wall are computed in the jet-related coordinates (x^*, z^*). The equation of the lines perpendicular to the surface and their angle with the horizontal direction are found. Then, the coordinates of the velocity profiles are computed in the curvilinear framework. Finally, the velocity values are linearly interpolated along the profile coordinates.

The analysed velocity profiles located in the diffusion zone of each actuator are shown in figures 8a and 8b for the plane and curved DBD-WJ respectively. Markers and line colors shown in the figures correspond to the ones employed all along the section at each given abscissa: the lighter the gray-scale color and the farther the profiles are in the jet streamwise direction.

	V_{AC} [kV]	b or b^* [mm]	U_j [m s^{-1}]	β [°]	Re_j	Re_N
Pos. A	18	4.8	2.8	-10	860	680
Pos. B	15	7.2	3.4	50	1600	1000
	18	7.7	3.8	60	1900	1200
Pos. C	15	5.7	3.0	70	1100	800
	18	6.2	3.3	70	1300	900
Plane DBD	15	2.5	2.8	-	450	-
	18	2.9	2.9	-	600	-

Table 3: DBD-WJ characteristics

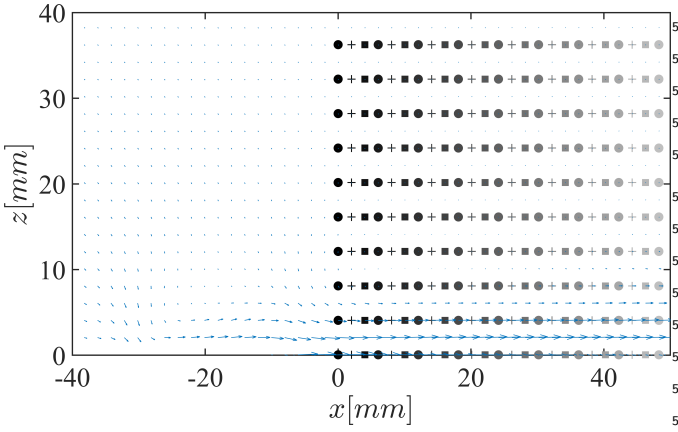

(a) Plane DBD

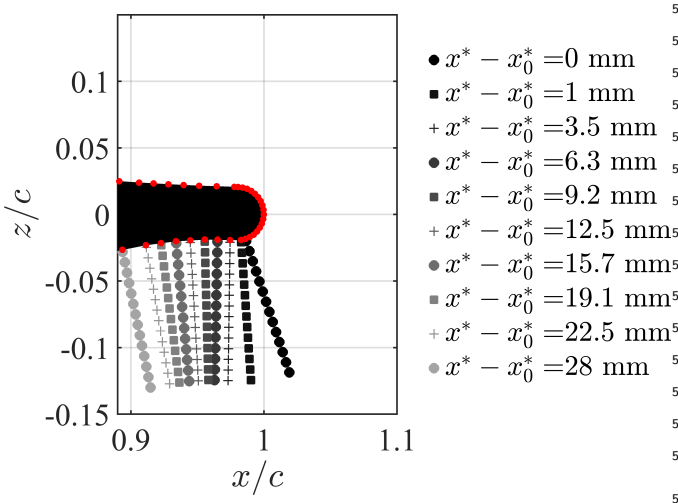

(b) Curved DBD

Figure 8: Location of the analysed velocity profiles and their respective markers

Dimensional profiles are shown in figure 9. The difference between the two DBD-WJs is clear as the plane induced jet is much thinner than its curved equivalent. The spread of the two configurations is also highlighted as the greater the x (or x^*) abscissa, the lower the maximum velocity and the higher the jet thickness for both DBD-WJs. In the case of the curved DBD case, the first three profiles in the streamwise direction (darker colors) are right after the virtual origin x_0^*. Their velocity values are near the maximum value U_j and the profiles show a high velocity gradient in the vicinity of the wall.

As suggested in Bradshaw and Gee (1960) the greater spread of the curved WJ can be induced by two factors: entrainment, necessary for jet attachment to the wall but also a source of jet destabilisation, and centrifugal forces acting on the flow. DBD induced jets have the same order of magnitude of maximum velocity but a strongly different topology (see figure 10a). Indeed, curved jets show a higher z_{max} and are much thicker, especially in the outer jet zone (*Pos. B* thicker than *Pos. C*). A centrifugal force density $f_{cent} = \rho\omega^2 r$ can be computed where $\omega = \frac{U}{r}$ is the angular velocity of the flow and r the radial position with respect to the center of the trailing-edge curvature. Figure 10b shows the f_{cent} profiles for the two curved actuators at the virtual origin x_0^*. The profiles clearly show that the centrifugal force is higher for the DBD-WJ in *Pos. B* along all the jet outer zone, highlighting the greater spread and the incipient separation from the wall. It seems that the centrifugal force acts mainly on the outer part of the WJ rather than on the inner part. As mentioned in Neuendorf and Wygnanski (1999), it can be assumed that, along with centrifugal forces, entrainment induces large eddies that provoke a rapid spreading of the DBD-WJ with a non-negligible vertical velocity component and a turbulence enhancement that leads to the WJ separation.

Figure 11a shows the flow rate $Q = \rho \int_{z=0}^{\infty} U(x,z)dz$ per unit length for the two actuators studied in this section and figure 11b the evolution of the local momentum flux J. In both curves the use of a multi DBD actuation is evidenced as Q and J increase in two distinct steps along the acceleration zone. In the case of the curved DBD-WJ, beyond the virtual origin, there is a flow rate and a momentum plateau highlighting an equilibrium between external mass entrainment and jet diffusion. In the case of the plane DBD-WJ, after the virtual origin there is a slight but steady flow rate increase and a momentum decrease. Hence, in the plane configuration, mass entrainment along the jet direction feeds the induced WJ, increasing its flow

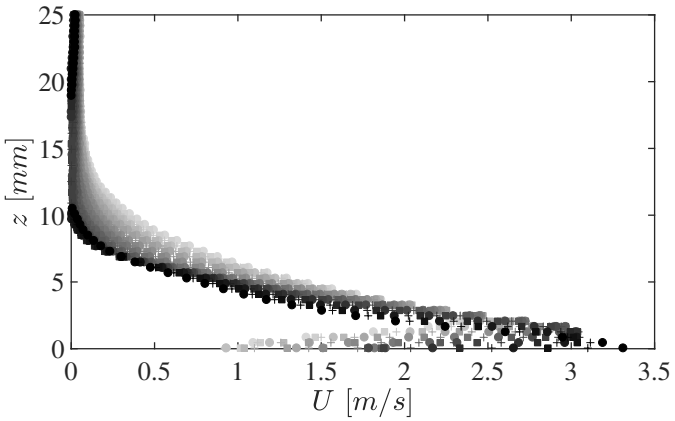

(a) Plane DBD (diffusion zone)

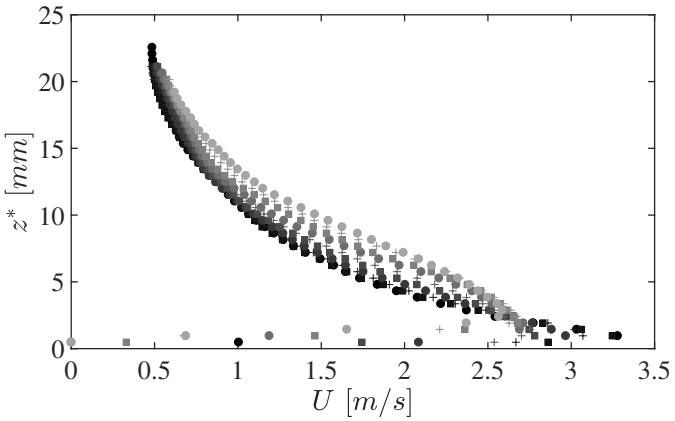

(b) Curved DBD (Pos. C - diffusion zone)

Figure 9: Dimensional velocity profiles at different x^* positions

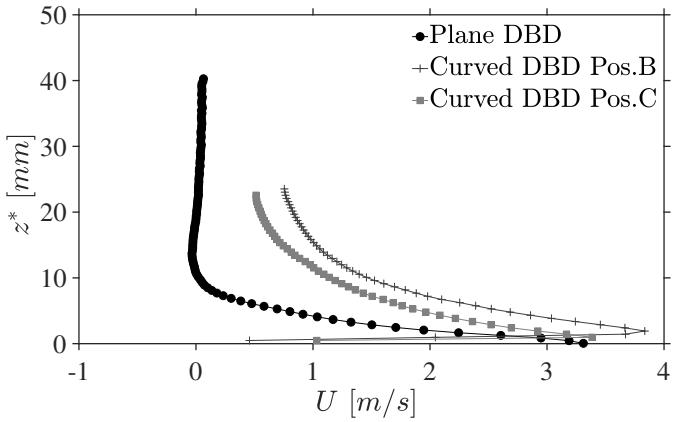

(a) Velocity U

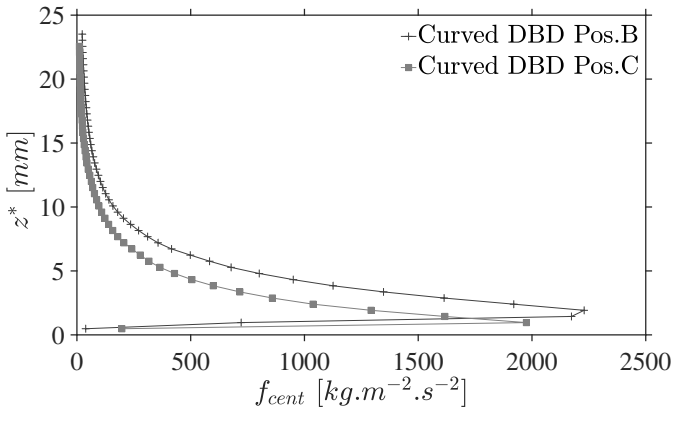

(b) Centrifugal force f_{cent}

Figure 10: Velocity U and centrifugal force f_{cent} profiles at the virtual origin x_0 (or x_0^*) for different actuators

rate and generating a momentum flux decrease.

The commonly used normalisation for velocity profiles is scaling 1 and the corresponding velocity profiles are plotted in figure 12. The plots also superimpose the laminar and turbulent cases obtained by Glauert and Schneider respectively. Regarding the plane DBD-WJ (figure 12a), this scaling collapses the experimental data reasonably well except the area in the very vicinity of the wall and the outer flow where the data scatter becomes larger. The ordinate of the maximum velocity is located at $\frac{z^*_{max}}{z^*_{\frac{1}{2}}} = 0.35$ right between the laminar and the turbulent profiles (0.6 for a laminar WJ, 0.15 to 0.2 for a turbulent WJ). (Boucinha et al., 2008b), Murphy et al. (2013) and Maden et al. (2013) studied the evolution of plane DBD induced jets and also found velocity profiles in between laminar and turbulent ones. The velocity gradient in the inner part seems closer to the laminar WJ, but the outer part tends to follow the turbulent velocity distribution. In the case of the curved DBD configuration (figure 12b), the profiles of the higher abscissas x^* (lighter colors) fit well the turbulent profile obtained by Schneider and Goldstein (1994) but the first velocity profiles beyond the virtual origin (darker colors) do not really fit either laminar or turbulent profiles, probably due to the EHD force existing for these profiles. However, the ordinate of $\frac{z^*_{max}}{z^*_{\frac{1}{2}}}$ is equal to 0.15 in agreement with the turbulent velocity profile. This first scaling does not perfectly collapse the mean velocity distribution in one single curve but a quasi-similarity is nonetheless reached. The ordinate of the maximum velocity peak confirms that DBD-WJs are in a transitional regime. The curved WJ matches the turbulent velocity profile for the higher abscissas x^* almost perfectly.

A second normalisation usually used in shear flows involving $z^*_{\frac{1}{2}}$, z^*_{max} and U_{max} is plotted in figure 13. This scaling has the characteristic of taking into account the increase in jet thickness. The normalisation does not collapse the data fully but is acceptable for the positive ordinates of the outer flow that tends to be similar to a free jet. In the inner region of the plane DBD induced jet, similarity is however not perfectly reached, particularly for the ordinates closer to the wall.

Figures 14 and 15 show velocity fluctuations and Reynolds stresses for plane and curved DBD-WJs respectively according to scaling 1. In the case of the plane DBD-WJ, self-similarity is clearly not obtained for the turbulent

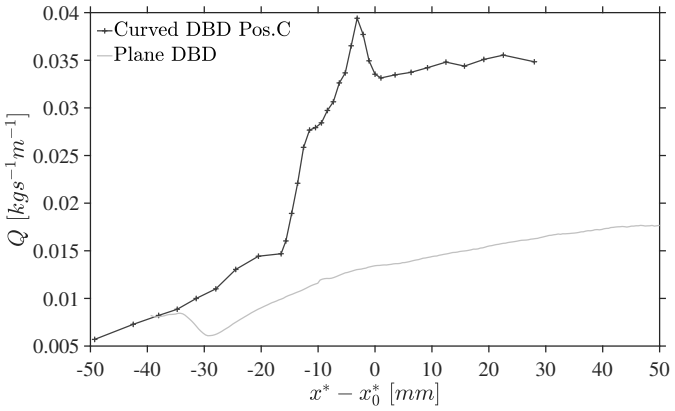

(a) Flow rate Q

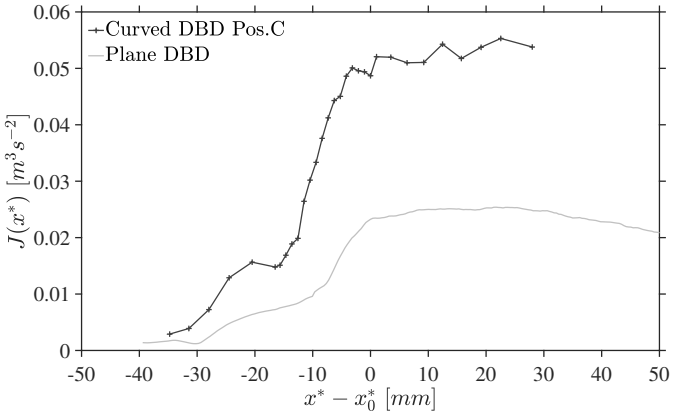

(b) Local momentum flux J

Figure 11: Flow rate and momentum flux evolution in the jet direction

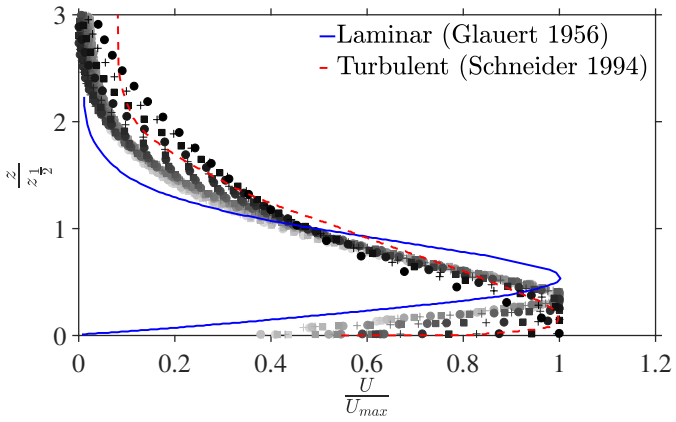

(a) Plane DBD (diffusion zone)

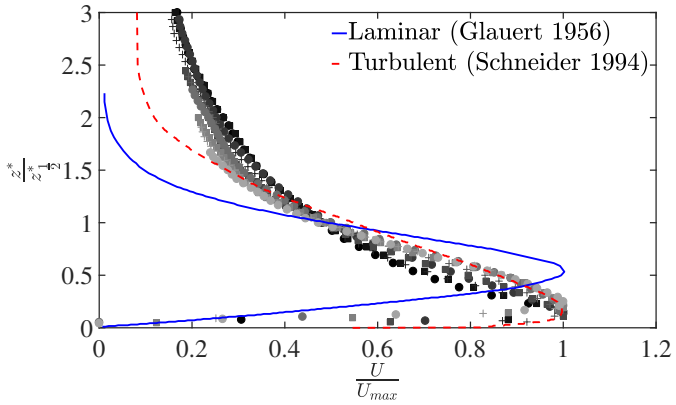

(b) Curved DBD (Pos. C - diffusion zone)

Figure 12: Normalised velocity profiles at different x^* positions based on scaling 1

contributions. The streamwise turbulence intensity $\frac{\sqrt{\overline{u'^2}}}{U_{max}}$ for the fluidic plane WJ shows theoretically two intensity peaks: one in the outer flow for a ratio $\frac{z^*}{z^*_{\frac{1}{2}}}$ equal to 0.7 and one in the inner layer, very close to the wall for a ratio equal to 0.03. Due to the low PIV resolution near the wall this second peak is not spatially resolved and not visible. All the profiles show a lower turbulence intensity than the fluidic plane WJ. Only the profiles at the end of the diffusion zone seem to reach the fluidic plane WJ profile (turbulence in the streamwise direction) or are the closest to it (turbulence in the normal direction). However, the turbulence peak at the end of the diffusion zone is located at roughly the same ordinates $\frac{z^*}{z^*_{\frac{1}{2}}}$ as the theoretical fluidic WJ as reported in table 4. The value of turbulence increases in the streamwise direction x for the three plotted stresses indicating that mixing and turbulence production increase in the x-direction as the jet develops and diffuses.

All the turbulence intensity profiles of the curved DBD-WJ (figure 15) show a higher turbulence magnitude than the fluidic plane WJ as mentioned in Neuendorf and Wygnanski (1999), in particular for turbulence intensity in the streamwise direction. Turbulence enhancement is due to

	$\frac{\sqrt{\overline{u'^2}}}{U_{max}}$	$\frac{\sqrt{\overline{v'^2}}}{U_{max}}$	$\frac{\sqrt{\overline{u'v'}}}{U_{max}}$
Wygnanski turbulent WJ	0.7	0.7	0.7
Plane DBD (end of the diffusion zone)	0.65	0.9	0.8
Curved DBD (end of the diffusion zone)	0.65	0.65	0.65

Table 4: Ordinates of turbulence intensity peaks

centrifugal forces acting on the jet that generates large eddies entraining the external air and inducing a broadening of the DBD-WJ. The ordinates of the maximum intensities are also shown in table 4. This ordinate increases progressively and stabilizes at a value of 0.65 for the three turbulence intensities plotted, remaining not very far from the 0.7 of the fluidic plane WJ. The level of turbulent fluctuations tends to increase up to a certain abscissa and then decreases. It is mainly visible for the normal component of turbulence and for the Reynolds stresses. This behaviour evidences the high jet spread and diffusion along the normal direction. However, it is clear that self-similarity of

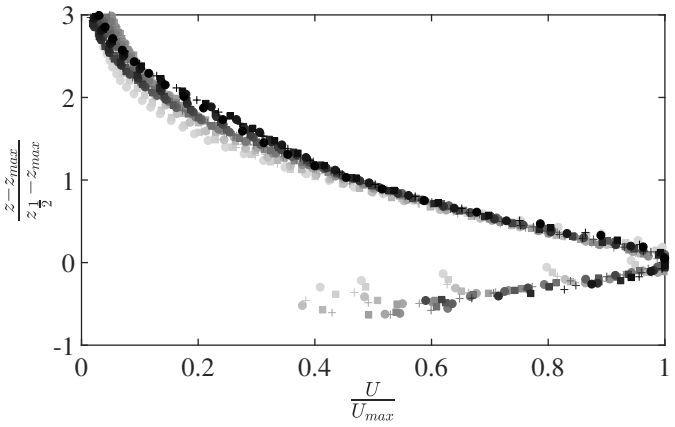

(a) Plane DBD (diffusion zone)

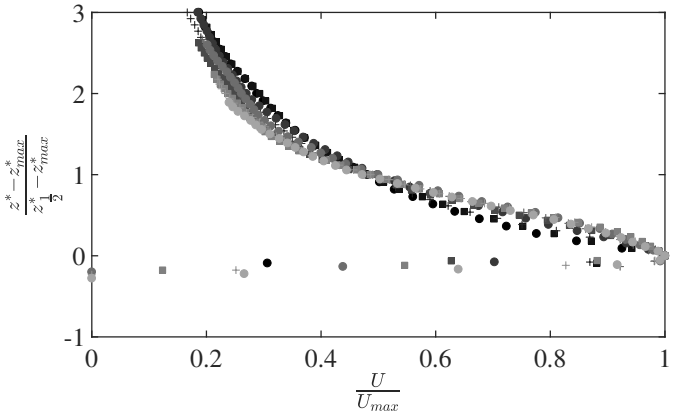

(b) Curved DBD (Pos. C - diffusion zone)

Figure 13: Normalised velocity profiles at different x^* positions (scaling based on $z^*_{\frac{1}{2}}$, z^*_{max} and U_{max})

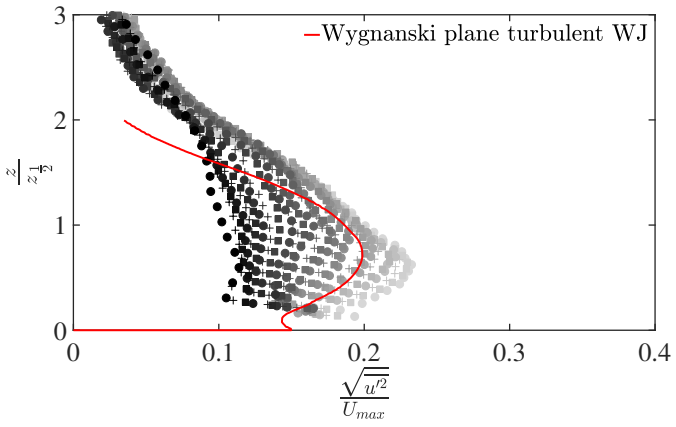

(a) Turbulence intensity in the streamwise direction

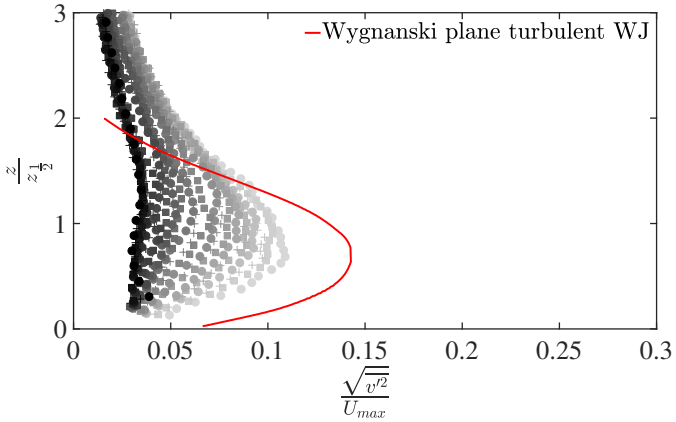

(b) Turbulence intensity in the normal direction

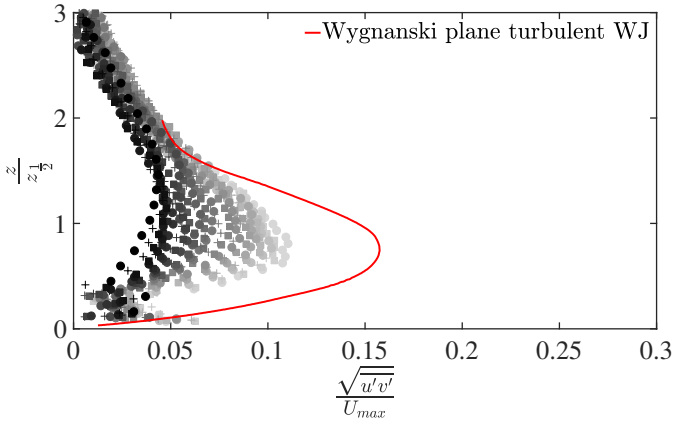

(c) Reynolds stresses

Figure 14: Turbulence intensities and Reynolds stresses at different x positions based on scaling 1 (plane DBD - diffusion zone)

turbulence intensity profiles is not obtained with this scaling and will not be obtained because of the noticeable decline in the turbulent components. This result was indeed expected because self-similarity of the mean flow is not completely obtained. However, the analysed velocity profiles are very close to the virtual origin (5 virtual slot widths for the curved DBD-WJ and 20 for the plane DBD-WJ) and these distances are not enough to properly characterise a WJ. Wygnanski et al. (1992) found self-similarity for the mean velocity profiles of their fluidic WJ but did not find it for the turbulent fluctuations with scaling 1. The authors conducted the experiments up to 120 slot widths downstream of the nozzle and admitted that this distance was not sufficient to attain self-similarity in their range of Reynolds numbers. Wilson and Goldstein (1976) in their study on the WJ around a cylinder did not find self-preservation of the turbulent quantities either, even though the mean flow appeared to be quasi-similar.

4.3. Transition to turbulence

The transition to turbulence of the induced jets is examined below regarding the DBD set-up and the possible flow instabilities.

Due to its sinusoidal nature, the DBD actuation produces a local unsteady force resulting from the distinct discharge regimes of positive and negative half cycles. Cohen et al. (1992) studied the laminar to turbulent transition of plane WJs and highlighted two unstable modes: an inviscid mode in the outer region driven by large spatial scales and a viscous mode characterised by small scale

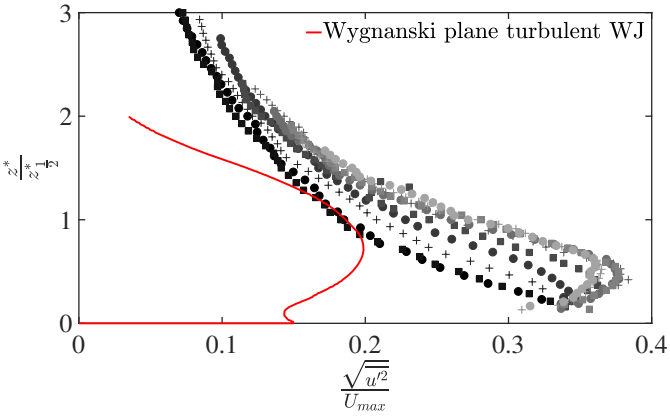

(a) Turbulence intensity in the streamwise direction

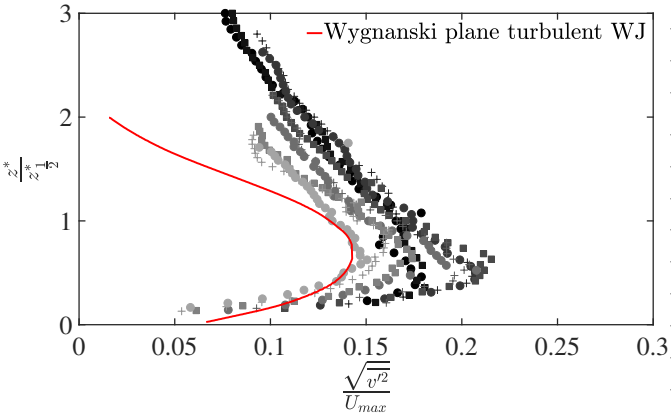

(b) Turbulence intensity in the normal direction

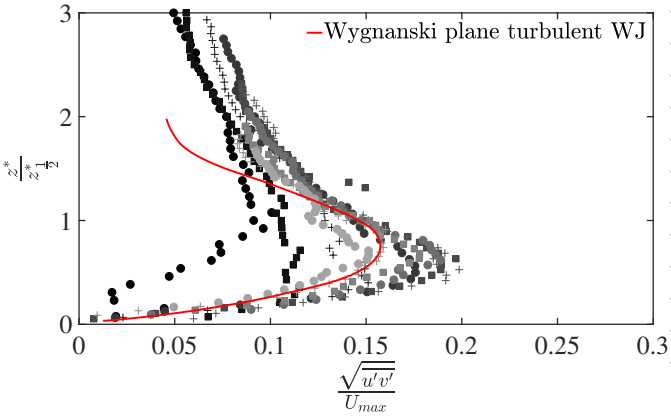

(c) Reynolds stresses

Figure 15: Turbulence intensities and Reynolds stresses at different x^* positions based on scaling 1 (curved DBD - diffusion zone)

disturbances in the inner region. At a distance from the nozzle of 15 slot widths and a $Re_j = 725$, these two modes have a reduced frequency $k = \frac{2\pi f z_{\frac{1}{2}}}{U_{max}}$ equal to 0.7 (inviscid) and 1.25 (viscous), f being the frequency of the instability. These values correspond to 56 Hz and 99 Hz respectively in the case of the plane DBD-WJ of the present study powered at $V_{AC} = 18$ kV. These natural instabilities of the present DBD induced jet have very low frequencies compared to the frequency of the actuation equal to 1 kHz. Therefore, it can be considered that, with the actuation, a quasi-steady momentum is produced and that the influence of the natural actuation unsteadiness f_{AC} on the laminar to turbulent transition is minor.

In addition to shear instabilities, shear flows over concave (or convex) walls are also subjected to an inviscid centrifugal instability quantified by the Rayleigh criterion that imposes $\frac{1}{r^3}\frac{d}{dr}\left(r^4\omega^2\right) > 0$ as a necessary and sufficient condition for stability. This instability generates streamwise oriented counter-rotating vortices, named Görtler vortices, that can lead the flow to transition to turbulence. This vortex motion is induced by the imbalance between the radial pressure gradient and the centrifugal force. As DBD-WJs have a non-monotonic velocity distribution of the velocity profiles, only the outer part of the WJs is unstable with respect to this centrifugal instability as mentioned in Floryan (1986) and Saric (1994). The calculation of the Görtler number $G = \frac{U_j\theta}{\nu}\left(\frac{\theta}{R}\right)^{\frac{1}{2}}$, where θ is the jet momentum thickness and R the radius of curvature of the surface gives, at the virtual origin, $G \approx 300$–350 for curved actuators leading to an unstable flow as reported in Floryan (1991). Regarding shear and considering the jet Reynolds numbers, DBD-WJs appear to be in a transitional regime whereas for centrifugal instabilities the induced flows are clearly unstable. Therefore, it can be assumed that Görtler instabilities are the primary instability mechanism of curved DBD induced flows.

Furthermore, the used serrated electrodes, which allow higher induced velocities than linear electrodes, generate small vortical structures with a lengthscale equal to the tooth spacing that convect downstream of the DBD-WJ and that locally modify the topology of the induced jets in the very vicinity of the active electrode. However, these structures are convected and dissipated beyond the electrodes and no well-established counter rotating vortices are formed (Joussot et al. (2013)) in the DBD-WJ inner layer where stabilising viscous effects exist. This spanwise forcing may be a factor for the existence of Görtler instabilities but the present PIV data cannot provide the means to address the transverse characteristics of the flow.

4.4. Jet evolution with dimensional variables

Four variables are used in this section to describe the DBD induced WJs evolution along the streamwise x-direction. The actuators are powered at a voltage $V_{AC} = 18$ kV and a frequency $f_{AC} = 1$ kHz. Figure 16a shows the evolution of z^*_{max} with x^* and figure 16b plots the evolution of $z^*_{\frac{1}{2}}$ with x^*. All the following variables are plotted with respect to the virtual origin x^*_0, the abscissa where the local jet velocity is maximal, meaning that $x^* - x^*_0 > 0$ corresponds to the jet diffusion zone. In the case of the plane DBD-WJ, a polynomial fitting is performed in the diffusion zone to address the low PIV resolution in the vertical direction. The three zones that distinguish a DBD induced jet can be identified. Aspiration is characterised

by a decrease of z^*_{max} and $z^*_{\frac{1}{2}}$. The acceleration zone corresponds to an almost constant z^*_{max} located very close to the wall and a progressive increase of $z^*_{\frac{1}{2}}$ revealing the induced WJ spread. Finally, after the virtual origin the jet does not accelerate anymore, becomes thicker, and diffuses along the model wall. This generates a progressive increase in z^*_{max} and consequently an increase in $z^*_{\frac{1}{2}}$.

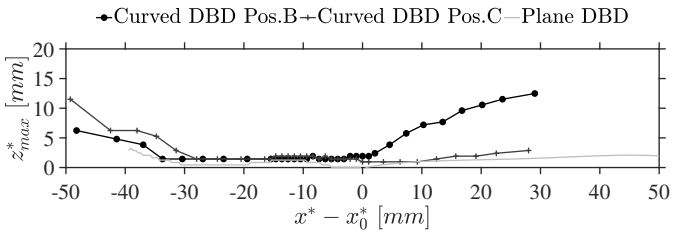

(a) Maximum velocity ordinate z^*_{max} evolution

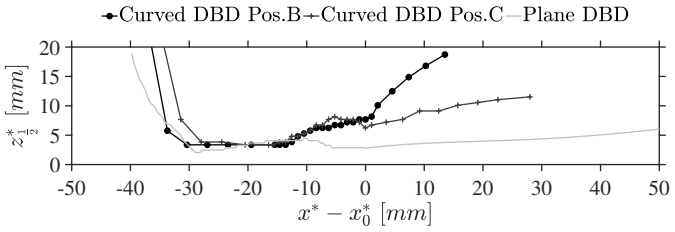

(b) Ordinate $z^*_{\frac{1}{2}}$ evolution

Figure 16: Maximum velocity ordinate z^*_{max} and ordinate $z^*_{\frac{1}{2}}$ evolution in the flow direction x^*

Due to the detached topology of the induced jet in *Pos. B*, z^*_{max} moves away from the wall right after the virtual origin. However, both the plane DBD-WJ and the curved DBD in *Pos. C* show a similar evolution of z^*_{max} especially in the diffusion zone. For these two attached jets, the actuator geometry, plane or curved, does not interfere in the ordinate of the maximum velocity that is close to 2.5 mm at the end of the diffusion zone actually visible in the PIV field of view. Regarding the evolution of the $z^*_{\frac{1}{2}}$ ordinate, curved DBD-WJs prove to have a higher spread than the plane one reaching 10 mm and 20 mm when their plane equivalent reaches 7 mm at the end of their respective diffusion zones. The induced jet in *Pos. B* reveals a spread that is twice as high as the one in *Pos. C* that is itself two times greater than the corresponding plane configuration. This evolution is in reasonable agreement with the results obtained by Bradshaw and Gee (1960) who found that the spread of a fluidic WJ over a cylinder is 1.5 times higher than over a flat plate.

Local maximum velocity $U_{max}(x^*)$ in the streamwise direction x^* is plotted in figure 17a. By definition, the velocity decay appears for all the actuators just beyond the virtual origin x^*_0. The maximum velocity is of the same order of magnitude for the three actuators plotted but the velocity decay is slower for the plane DBD-WJ. For this jet, the multi-DBD actuation is clearly visible as the velocity increases in two stages: a first stage up to 1.8 m/s and a second stage up to 3.3 m/s. A two-step velocity increase is also visible for the curved flows whose velocity gap between the two single-DBDs is about 0.5 m/s to 1 m/s.

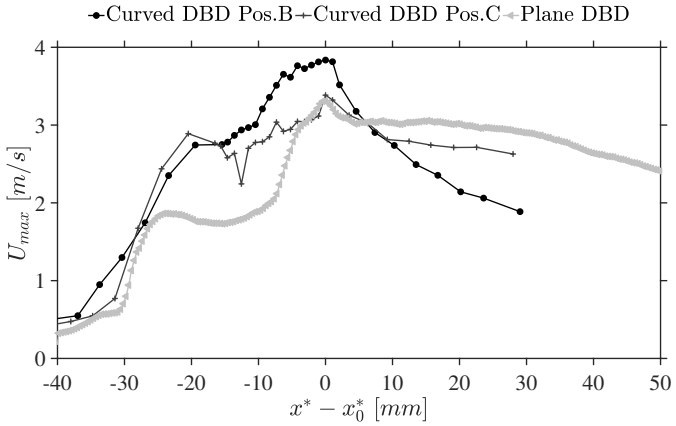

(a) Maximum velocity U_{max} evolution

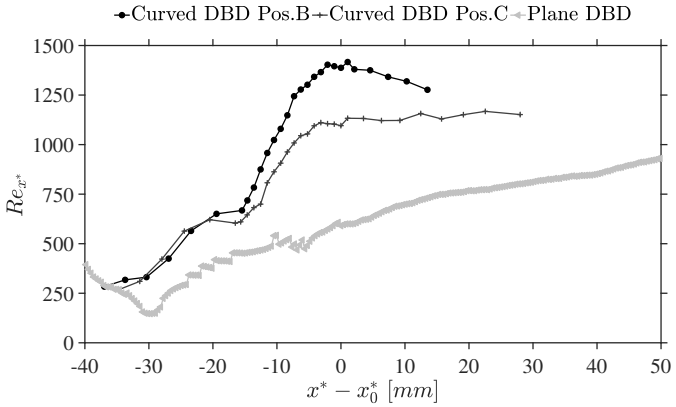

(b) Local Reynolds number Re_{x^*} evolution

Figure 17: Maximum velocity U_{max} and local Reynolds number Re_{x^*} evolution in the flow direction x^*

The evolution of the local Reynolds number Re_{x^*} with x^* is shown in figure 17b. In the case of the plane DBD-WJ, the increase in the Reynolds number begins over the first actuator ($x^* - x^*_0 \in [-30, -20]$) and Re_{x^*} continues to grow past the virtual origin at a relatively constant pace. This happens because the spread is greater than the velocity decay in the diffusion zone inducing a Re_j increase up to 900. The curved DBD-WJ in *Pos. B* shows a slight decrease after the virtual origin because its velocity decrease is greater than the rate of spread increase. The curved DBD-WJ in *Pos. C* shows a Reynolds number plateau in the diffusion zone. For both curved jets, the Reynolds number increases in two distinct steps that again highlight the implementation of multi-DBD actuators. Because of the greater thickness of curved DBD-WJs, their overall Re_{x^*} level is greater than for the plane DBD induced jet.

The electrode arrangement is identical for the three actuators studied, the only distinct parameter is the geometry of the actuator basis (curved or plane) and the position

of the electrodes around the curvature when the surface is curved. These results suggest that there is an effect of the surface curvature on the jet development specially in terms of rate of spread that more than doubles for the curved jet compared to its plane equivalent.

4.5. Jet evolution with normalised variables

A wall jet development over a surface can be characterised by the evolution of two main parameters: the maximum velocity decay and the rate of spread. The three scaling laws explained in table 2 were applied to the present experimental data in order to characterise the streamwise evolution of DBD induced jets in the diffusion zone solely. Concerning scaling 1 and as pointed out by Förthmann (1936), the decay of the maximum jet velocity is expected to vary as $x^{-\frac{1}{2}}$. In order to accentuate the decay, the ratio $\left(\frac{U_j}{U_{max}}\right)^2$ is commonly plotted versus $\frac{x^*-x_0^*}{b^*}$ and is shown in figure 18a for the diffusion zone only i.e. $x^*-x_0^*>0$. Figure 18b shows the rate of spread in the streamwise direction i.e. $\frac{z^*_{\frac{1}{2}}}{b^*}$ as a function of $\frac{x^*-x_0^*}{b^*}$. Maximum velocity decay and rate of spread can be expressed by the following power laws (equations 6 and 7 respectively) where A_u and A_z are constants summarised in table 5.

$$\left(\frac{U_j}{U_{max}}\right)^2 = A_u\left(\frac{x^*-x_0^*}{b^*}\right) \tag{6}$$

$$\frac{z^*_{\frac{1}{2}}}{b^*} = A_z\left(\frac{x^*-x_0^*}{b^*}\right) \tag{7}$$

	Re_j	A_u	A_z
Curved DBD Pos. B	1900	0.80	0.87
Curved DBD Pos. C	1300	0.19	0.22
Plane DBD	600	0.04	0.06
Wygnanski et al. (1992)	3400	0.15	0.09

Table 5: Table summarizing slope values A_u and A_z of the power laws in equations 6 and 7

After the virtual origin x_0^*, the evolution of $\left(\frac{U_j}{U_{max}}\right)^2$ is linear for both curved and plane DBD-WJs confirming the theoretical $x^{-\frac{1}{2}}$ evolution of the velocity decay. In the same way, the rate of spread of DBD induced jets behaves as a classical fluidic WJ and evolves linearly in the diffusion zone. DBD curved WJs exhibit a much higher velocity decay than the plane DBD and a higher rate of spread as well. The effect of the jet Reynolds number is significant in the present study. The higher the Re_j, the higher the slopes A_u and A_z. For instance, the slopes of the actuator in *Pos. B* are more than 10 times higher than the ones concerning the plane WJ. There is, indeed, a Reynolds number effect arising from the jet thickness b^*, itself directly related to the electrode position around the TE and to the jet topology. This Re_j evolution is not in agreement with the results obtained by Wygnanski et al. (1992) who found an opposite behaviour for a classical fluidic plane WJ. However, DBD induced jets are different in nature to purely fluidic ones and comparisons should be made carefully.

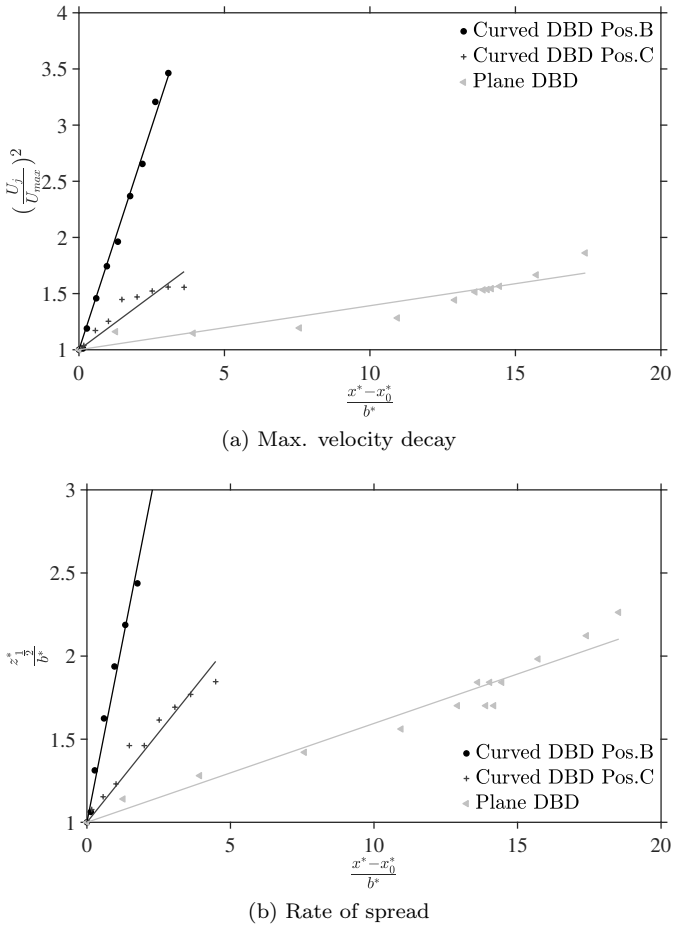

(a) Max. velocity decay

(b) Rate of spread

Figure 18: Maximum velocity decay and rate of spread in the flow direction based on scaling 1 (diffusion zone)

A second scaling involving the kinematic momentum flux J and the kinematic viscosity ν (scaling 2) is introduced. This scaling arises from Narasimha et al. (1973) who suggested that a fully developed WJ should attain an equilibrium independent of the nozzle conditions (such as b^*) and only dependent on the kinematic momentum flux at the nozzle J_0. As self-similarity of the mean flow is not completely reached in the present study, scaling 2 was used with the local momentum flux $J(x^*)$. The same plots with a scaling based on J_0 do not add any supplementary information to the analysis. The corresponding scaling values for the velocity decay and rate of spread evolution

are $\frac{U_{max}\nu}{J(x^*)}$ and $\frac{z^*_{\frac{1}{2}}\,J(x^*)}{\nu^2}$, whereas the streamwise direction evolves as $\frac{(x^*-x_0^*)J(x^*)}{\nu^2}$. Figures 19a and 19b show the velocity decay and the rate of spread respectively in the streamwise direction. All the plotted experimental points correspond to the diffusion zone of the induced WJs. Scaling 2 does not collapse the streamwise behaviour of the three DBD induced jets. Evolutions of the rate of spread and of the maximum velocity decay are roughly linear and their slopes are not very far from each other. However, the three curves are not superimposed, implying that the kinematic momentum flux is not a valid parameter for the normalisation of DBD-WJs evolution. The curves suggest that the kinematic momentum flux is not the only parameter that drives the jet spread and velocity decay.

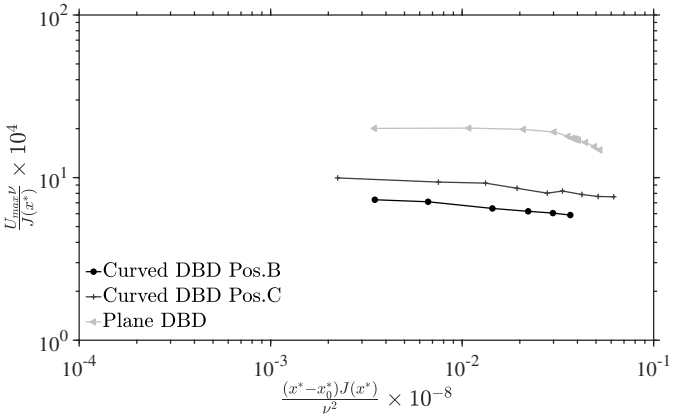

(a) Max. velocity decay

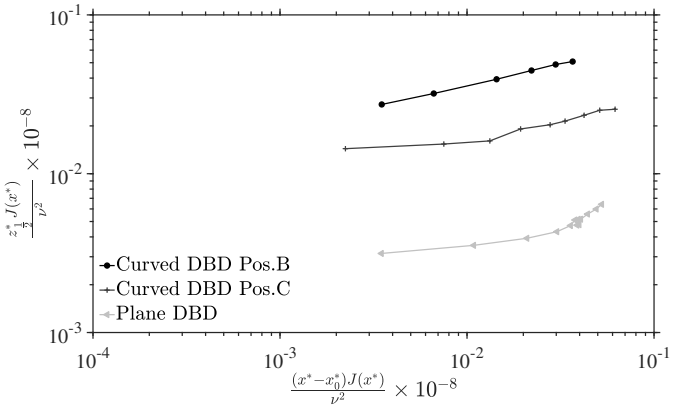

(b) Rate of spread

Figure 19: Maximum velocity decay and rate of spread in the flow direction based on scaling 2 (diffusion zone)

A third scaling suggested by Neuendorf and Wygnanski (1999) for the wall jet developing around a circular cylinder and involving the radius of curvature R (scaling 3) was used. Indeed, when the ratio $\frac{b^*}{R}$ is not small the length scale R has real meaning. In the present investigation, b^* is of the same order of magnitude as R. In this way, $\frac{U_{max}}{(J(x^*)/R)^{\frac{1}{2}}}$ is plotted in figure 20a for the characterisation of the velocity decay and $\frac{z^*_{\frac{1}{2}}}{R}$ in figure 20b for the evaluation of the rate of spread. The evolution of these variables is plotted as a function of $\frac{(x^*-x_0^*)}{R}$. This scaling collapses the two curves for the velocity decay reasonably well, suggesting that the radius of curvature is an important length scale of the curved DBD-WJs even in the diffusion zone and after the effective curvature. The scaling seems less relevant for the characterisation of the rate of spread evolution, since the actuator in *Pos. B* shows a greater spread than the one in *Pos. C* with this normalisation as well. However, for both jets, the rate of spread seems to follow a square evolution.

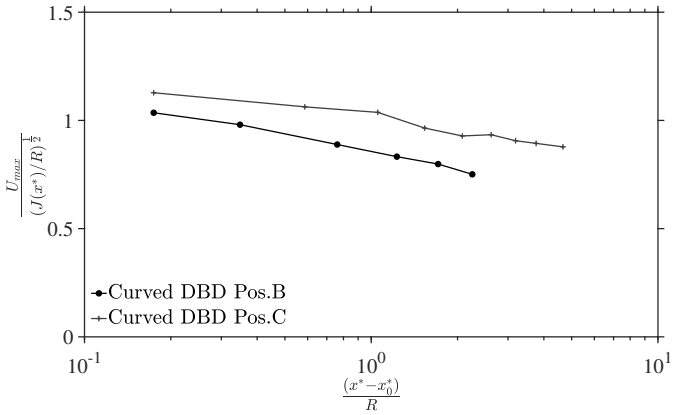

(a) Maximum velocity decay

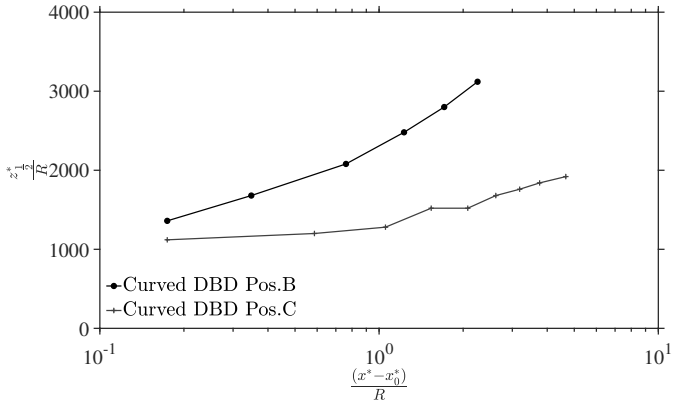

(b) Rate of spread

Figure 20: Maximum velocity decay and rate of spread in the flow direction based on scaling 3 (diffusion zone)

5. Conclusion

The present work dealt with transitional DBD induced jets developing over curved surfaces and studied in the framework of an experimental circulation control application, carried out by acting near a rounded trailing-edge of an airfoil. The same DBD configuration was employed on a plane configuration and on three curved configurations where the electrodes were placed along the rounded trailing-edge.

Time averaged velocity fields from PIV measurement in quiescent air conditions allowed to assess the evolution of these flows. Firstly, they show that the electrode position around the curvature has a direct impact on the jet topology and particularly on whether the induced jet is going to follow the model curvature or not. The configuration where the zone of EHD interaction reaches the end of the curvature allows a complete adhesion of the induced jet to the wall. The reason why the wall jet stays attached to the wall seems to be more an electrical effect than a phenomenon due to the dynamics of the fluid. A possible Coanda effect is not applicable in this study as the Reynolds numbers of the induced jets are small and the jet thicknesses are large compared to the common cases of jet adhesion to a curved surface. Secondly, compared to plane DBD wall jets, curved DBD wall jets experience centrifugal effects. Wall curvature induces higher wall jets thicknesses and rates of spread in the diffusion zone leading to an important entrainment of the outer flow. Such as for fluidic wall jets along a cylinder, the radius of curvature of the wall is an important length scale to describe the DBD wall jet evolution, more particularly with regard to the velocity decay. Compared to plane DBD wall jets in which shear instabilities drive the transition mechanism, it seems that, for curved DBD wall jets, transition is likely triggered by the centrifugal instabilities taking place especially in the outer jet area. When comparing the main features of DBD wall jets in the diffusion zone to canonical fluidic wall jets, plane and curved DBD induced jets show a similar velocity decay and rate of spread evolution in the streaming direction, expected to vary as $x^{-\frac{1}{2}}$ and linearly respectively. Regarding the self-similarity of the mean velocity profiles along the streaming direction, a quasi-similarity can be observed in the diffusion zone but self-similarity of the turbulent components is not obtained and cannot be obtained because of the noticeable and quick decline of the fluctuation components before the jet dissipation or separation. Indeed, due to their inherent limitation to produce high velocity flows, the jet Reynolds numbers of DBD wall jets remain very low, in the range of laminar or transitional jets, compared to the common Reynolds numbers of fluidic wall jets. Thus, it can be assumed that DBD cannot induce fully developed turbulent jets.
Conducting this study in the presence of an external flow would probably reveal other aspects of the evolution properties of DBD wall jets, as for fluidic wall jets. This approach remains a challenge as discussed in Pereira et al. (2014), more particularly to consider accurately the wall shear changes.

Acknowledgements

This project was funded by the French national project SMARTEOLE (ANR-14-CE05-0034). The authors want to thank the reviewers for their comments which helped to improve the quality of the paper.

References

R.A. Bajura and M.R. Catalano. Transition in a two-dimensional plane wall jet. *Journal of Fluid Mechanics*, 9:199–216, 1971. doi:10.1017/S0022112075002340.

R.A. Bajura and A.A. Szewczyk. Experimental investigation of a laminar two-dimensional plane wall jet. *The Physics of Fluids*, 13 (7):1653–1664, 1970. doi:10.1063/1.1693137.

N. Balcon, N. Benard, and E. Moreau. Formation process of the electric wind produced by a plasma actuator. *IEEE Transactions on Dielectrics and Electrical Insulation*, 16(2):463–469, 2009. doi:10.1109/TDEI.2009.4815179.

S. Baleriola, A. Leroy, S. Loyer, P. Devinant, and S. Aubrun. Circulation control on a rounded trailing-edge wind turbine airfoil using plasma actuators. *Journal of Physics: Conference Series*, 753(5):052001, 2016. doi:10.1088/1742-6596/753/5/052001.

M. Belan and F. Messanelli. Compared ionic wind measurements on multi-tip corona and DBD plasma actuators. *Journal of Electrostatics*, 76, 08 2015. doi:10.1016/j.elstat.2015.06.008.

N. Benard and E. Moreau. Electrical and mechanical characteristics of surface AC dielectric barrier discharge plasma actuators applied to airflow control. *Experiments in Fluids*, 2014. doi:10.1063/1.4712125.

N. Benard, A. Mizuno, and E. Moreau. A large-scale multiple dielectric barrier discharge actuator based on an innovative three-electrode design. *Journal of Physics D: Applied Physics*, 42(23): 235204, 2009. doi:10.1088/0022-3727/42/23/235204.

J.P. Boeuf, Y. Lagmich, Th. Unfer, Th. Callegari, and L.C. Pitchford. Electrohydrodynamic force in dielectric barrier discharge plasma actuators. *Journal of Physics D: Applied Physics*, 40(3): 652, 2007. doi:10.1088/0022-3727/40/3/S03.

V. Boucinha, P. Magnier, B. Dong, R. Weber, and A. Leroy. Plasma flow control: characterization of the ionic wind in still air by laser doppler velocimetry (LDV). *13th Int. Symposium on Flow Visualization*, 2008a.

V. Boucinha, P. Magnier, A. Leroy, R. Weber, R. Joussot, B. Dong, and D. Hong. Characterization of the ionic wind induced by a sine DBD actuator used for laminar-to-turbulent transition delay. *4th AIAA Flow Control Conference*, 4210, 2008b. doi:10.2514/6.2008-4210.

P. Bradshaw and M.T. Gee. Turbulent Wall Jets with and without an External Stream. *Aeronautical Research Council Reports and Memoranda*, pages 1–48, 1960.

D.H. Chun and W.H. Schwarz. Stability of the plane incompressible viscous wall jet subjected to small disturbances. *The Physics of Fluids*, 10(5):911–915, 1967. doi:10.1063/1.1762241.

J. Cohen, M. Amitay, and B. J. Bayly. Laminar turbulent transition of wall jet flows subjected to blowing and suction. *Physics of Fluids A: Fluid Dynamics*, 4(2):283–289, 1992. doi:10.1063/1.858304.

H.W. Coleman and W.G. Steele. *Experimentation, Validation, and Uncertainty Analysis for Engineers*. John Wiley & Sons, Inc., 3rd edition edition, 2009. ISBN 9780470168882.

A. Debien, R. Sosa, N. Benard, and E. Moreau. Electric wind produced by sliding discharges. *2nd ISNPEDADM new electrical technologies for environement*, 01 2011.

R. Durscher and S. Roy. Evaluation of thrust measurement techniques for dielectric barrier discharge actuators. *Experiments in Fluids*, 53(4):1165–1176, 2012. doi:10.1007/s00348-012-1349-6.

R. Erfani, H. Zare-Behtash, and K. Kontis. Plasma actuator: Influence of dielectric surface temperature. *Experimental Thermal and Fluid Science*, 42:258 – 264, 2012. ISSN 0894-1777. doi:10.1016/j.expthermflusci.2012.04.023.

G.I. Fekete. Coanda flow of a two-dimensional wall jet on the outside of a circular cylinder. *Report (McGill University. Mechanical Engineering Research Laboratories) 63-11*, 1963.

L.-H. Feng, K.-S. Choi, and J.-J. Wang. Flow control over an air-foil using virtual gurney flaps. *Journal of Fluid Mechanics*, 767:595–626, 2015. doi:10.1017/jfm.2015.22.

J.M. Floryan. Görtler instability of boundary layers over concave and convex walls. *The Physics of Fluids*, 29(8):2380–2387, 1986. doi:10.1063/1.865531.

J.M. Floryan. On the Görtler instability of boundary layers. *Progress in Aerospace Sciences*, 28(3):235 – 271, 1991. doi:10.1016/0376-0421(91)90006-P.

M. Forte, J. Jolibois, J. Pons, E. Moreau, G. Touchard, and M. Cazalens. Optimization of a dielectric barrier discharge actuator by stationary and non-stationary measurements of the induced flow velocity: Application to airflow control. *Experiments in Fluids*, 43(6):917–928, 2007. doi:10.1007/s00348-007-0362-7.

E Förthmann. *Turbulent jet expansion*. National Advisory Committee for Aeronautics, Technical Memorandumm No. 789, Washington, USA, 1936.

M.B. Glauert. The wall jet. *Journal of Fluid Mechanics*, 1(06):625, 1956. ISSN 0022-1120. doi:10.1017/S002211205600041X.

R.D. Joslin and G.S. Jones. *Applications of Circulation Control Technology (Progress in Astronautics and Aeronautics)*. AIAA, 2006.

R. Joussot, A. Leroy, R. Weber, H. Rabat, S. Loyer, and D. Hong. Plasma morphology and induced airflow characterization of a dbd actuator with serrated electrode. *Journal of Physics D: Applied Physics*, 46(12):125204, 2013. doi:10.1088/0022-3727/46/12/125204.

T. Jukes, K.S. Choi, G. Johnson, and S. Scott. Turbulent boundary layer control for drag reduction using surface plasma. *2nd AIAA Flow Control Conference*, 2216, 2006. doi:10.2514/6.2004-2216.

A. Kaffel, J. Moureh, J.L. Harion, and S. Russeil. Experimental investigation of a plane wall jet subjected to an external lateral flow. *Experiments in Fluids*, 56(5):1–19, 2015. ISSN 07234864. doi:10.1007/s00348-015-1969-8.

R.D. Keane and R.J. Adrian. Optimization of particle image velocimeters. I. Double pulsed systems. *Measurement science and technology*, 1(11):1202, 1990.

M. Kotsonis. Diagnosis for characterization of plasma actuators. *Measurement Science and Technology*, 26(9):092001, 2015. doi:10.1088/0957-0233/26/9/092001.

M. Kotsonis, R. Pul, and L. Veldhuis. Influence of circulation on a rounded-trailing-edge airfoil using plasma actuators. *Exp. in Fluids*, 55(7), 2014. doi:10.1007/s00348-014-1772-y.

J. Kriegseis, B. Simon, and S. Grundmann. Towards in-flight applications? a review on dielectric barrier discharge-based boundary layer control. *ASME. Appl. Mech. Rev.*, 68(2), 2016. doi:10.1115/1.4033570.

E.F. Kurtz and S.H. Crandall. Computer-aided analysis of hydrodynamic stability. *Journal of Mathematics and Physics*, 41(1-4):264–279, 1962. ISSN 1467-9590. doi:10.1002/sapm1962411264.

E.N. Lovig, R.S. Downs, and E.B. White. Passive laminar flow control at low turbulence levels. *AIAA Journal*, 52(5):1072–1075, 2014. doi:10.2514/1.J052363.

I. Maden, R. Maduta, J. Kriegseis, S. Jakirlić, C. Schwarz, S. Grundmann, and C. Tropea. Experimental and computational study of the flow induced by a plasma actuator. *International Journal of Heat and Fluid Flow*, 41:80 – 89, 2013. ISSN 0142-727X. doi:10.1016/j.ijheatfluidflow.2013.02.013.

T. Matsuno, M. Sugahara, H. Kawazoe, and H. Nishida. Development of serrated multi-electrode plasma actuators for enhanced force production. *54th AIAA Aerospace Sciences Meeting*, 2016. doi:10.2514/6.2016-1691.

J.A.W. Meijerink and H.W.M. Hoeijmakers. Plasma actuators for active flow control on wind turbine blades. *29th AIAA Applied Aerodynamics Conference*, pages 1–18, 2011. doi:10.2514/6.2011-3353.

E. Moreau. Airflow control by non-thermal plasma actuators. *Journal of Physics D: Applied Physics*, 40:605–636, 2007. doi:10.1088/0022-3727/40/3/S01.

E. Moreau, C. Louste, and G. Touchard. Electric wind induced by sliding discharge in air at atmospheric pressure. *Journal of Electrostatics*, 66:pp. 107–114, 2008. doi:10.1016/j.elstat.2007.08.011.

J. P. Murphy, J. Kriegseis, and P. Lavoie. Scaling of maximum velocity, body force, and power consumption of dielectric barrier discharge plasma actuators via particle image velocimetry. *Journal of Applied Physics*, 113(24):243301, 2013. doi:10.1063/1.4811225.

R. Narasimha, K. Yegna Narayan, and S.P. Parthasarathy. Parametric analysis of turbulent wall jets in still air. *The Aeronautical Journal*, 77(751):355–359, 1973. doi:10.1017/S0001924000041324.

R. Neuendorf and I. Wygnanski. On a turbulent wall jet flowing over a circular cylinder. *Journal of Fluid Mechanics*, 381:1–25, 1999. ISSN 00221120. doi:10.1017/S0022112098003668.

R. Pereira, D. Ragni, and M. Kotsonis. Effect of external flow velocity on momentum transfer of dielectric barrier discharge plasma actuators. *Journal of Applied Physics*, 116(10):103301, 2014. doi:10.1063/1.4894518.

J. Pons, E. Moreau, and G. Touchard. Asymmetric surface dielectric barrier discharge in air at atmospheric pressure: electrical properties and induced airflow characteristics. *Journal of Physics D: Applied Physics*, 38(19):3635–3642, 2005. doi:10.1088/0022-3727/38/19/012.

M.L. Post and T.C. Corke. Separation control on high angle of attack airfoil using plasma actuators. *AIAA Journal*, 42(11):2177–2184, 2004. doi:10.2514/1.2929.

A.K. Prasad. Particle Image Velocimetry. *Current Science*, 79(1):51–60, 2000.

F. Rogier, G. Dufour, and K. Kourtzanidis. Numerical Simulation of sinusoidal DBD actuators and comparison with experiments. *45th AIAA Plasmadynamics and Lasers Conference*, 2014. doi:10.2514/6.2014-2808.

J. Roth, R.C.M. Madhan, M. Yadav, J. Rahel, and S. Wilkinson. Flow field measurements of paraelectric, peristaltic, and combined plasma actuators based on the one atmosphere uniform glow discharge plasma. *42nd AIAA Aerospace Sciences Meeting and Exhibit*, 0845, 2004. doi:10.2514/6.2004-845.

W.S. Saric. Görtler vortices. *Annual Review of Fluid Mechanics*, 26(1):379–409, 1994. doi:10.1146/annurev.fl.26.010194.002115.

M. E. Schneider and R. J. Goldstein. Laser doppler measurement of turbulence parameters in a two dimensional plane wall jet. *Physics of Fluids*, 6(9):3116–3129, 1994. doi:10.1063/1.868136.

C.Y. Schuele, T.C. Corke, and E. Matlis. Control of stationary cross-flow modes in a mach 3.5 boundary layer using patterned passive and active roughness. *Journal of Fluid Mechanics*, 718:5–38, 2013. doi:10.1017/jfm.2012.579.

W. Shyy, B. Jayaraman, and A. Andersson. Modeling of glow discharge-induced fluid dynamics. *Journal of Applied Physics*, 92(11):6434–6443, 2002. doi:10.1063/1.1515103.

R. Sosa, G. Artana, E. Moreau, and G. Touchard. Stall control at high angle of attack with plasma sheet actuators. *Experiments in Fluids*, 42(1):143–167, 2007. doi:10.1007/s00348-006-0227-5.

Y. Suzen, G. Huang, J. Jacob, and D. Ashpis. Numerical simulations of plasma based flow control applications. *35th AIAA Fluid Dynamics Conference and Exhibit*, 2005. doi:10.2514/6.2005-4633.

T. Van Hooff, B. Blocken, T. Defraeye, J. Carmeliet, and G.J.F. Van Heijst. PIV measurements of a plane wall jet in a confined space at transitional slot Reynolds numbers. *Experiments in Fluids*, 53(2):499–517, 2012. ISSN 07234864. doi:10.1007/s00348-012-1305-5.

T. Vít and F. Maršík. Experimental and theoretical study of heated coanda jet. *21st International Congress of Theoretical and Applied Mechanics*, 2004.

D.J. Wilson and R.J. Goldstein. Turbulent wall jets with cylindrical streamwise surface curvature. *Journal of Fluids Engineering*, 98, 1976. doi:10.1115/1.3448393.

I. Wygnanski, Y. Katz, and E. Horev. On the applicability of various scaling laws to the turbulent wall jet. *Journal of Fluid Mechanics*, 234(-1):669, 1992. ISSN 0022-1120. doi:10.1017/S002211209200096X.

S. Yadala, M.T. Hehner, J. Serpieri, N. Benard, P.C. Dörr, M.J. Kloker, and M. Kotsonis. Experimental control of swept-wing transition through base-flow modification by plasma actuators. *Journal of Fluid Mechanics*, 844:R2, 2018. doi:10.1017/jfm.2018.268.

P. Zhang, B. Yan, A.B. Liu, and J.J. Wang. Numerical simulation on plasma circulation control airfoil. *AIAA Journal*, 48(10):2213–2226, 2010. doi:10.2514/1.J050133.

X. Zhang, P. Chen, and X. Luo. Airfoil flow control using plasma actuation and coanda effect. *29th AIAA Applied Aerodynamics Conference*, 2011. doi:10.2514/6.2011-3516.